Asian Power Electronics Journal

PERC, HK PolyU

First edition June. 2019 Printed in Hong Kong by Reprographic Unit
The Hong Kong Polytechnic University

Published by

Power Electronics Research Centre
The Hong Kong Polytechnic University
Hung Hom, Kowloon, Hong Kong

ISSN 1995-1051

Editorial board

Honorary Editor

Prof. Fred C. Lee Electrical and Computer Engineering, Virginia Polytechnic Institute and State University

Editor

Prof. Yim-Shu Lee
Victor Electronics Ltd.

Associate Editors and Advisors

Prof. Philip T. Krien
Department of Electrical and Computer Engineering, University of Illinois

Prof. Keyue Smedley
Department of Electrcial and Computer Engineering, University of California

Prof. Muhammad H. Rashid
Department of Electrical and Computer Engineering, University of West Florida

Prof. Dehong Xu
College of Electrical Engineering, Zhejiang University

Prof. Hirofumi Akagi
Department of Electrical Engineering, Tokyo Institute of Technology

Prof. Xiao-zhong Liao
Department of Automatic Control, Beijing Institute of Technology

Prof. Hao Chen
Dept. of Automation, China University of Mining and Technology

Prof. Danny Sutanto
Integral Energy Power Quality and Reliability Centre, University of Wollongong

Prof. S.L. Ho
Department of Electrical Engineering, The Hong Kong Polytechnic University

Prof. Eric K.W. Cheng
Department of Electrical Engineering, The Hong Kong Polytechnic University

Dr. Norbert C. Cheung
Department of Electrical Engineering, The Hong Kong Polytechnic University

Dr. Edward W.C. Lo
Department of Electrical Engineering, The Hong Kong Polytechnic University

Dr. Martin H.L. Chow
Department of Electronic and Information Engineering, The Hong Kong Polytechnic University

Dr. Chi Kwan Lee
Department of Electrical and Electronic Engineering, The University of Hong Kong

Table of Content

Asian Power Electronics Journal, Vol. 13 , No.1, June 2019

A Switched-capacitor Step-up Inverter for Bidirectional Wireless Charging Applications in Electric Microcar

Fong Y. C [1] Cheng K. W. E [2]

Abstract–Wireless power transfer (WPT) offers a more convenient and safer option for electric vehicle (EV) charging. However, the mismatch of the DC link voltages between the charging stations and small scale EVs may increase the difficulty of design and control of the charging facilities. Along with the growing penetration of renewable energy, vehicle-to-buildings (V2B) and vehicle-to-grid (V2G) interfaces, requiring bidirectional power flow would be the essential features of future EV wireless charging systems. In order to tackle this issue, this paper suggests a high-frequency step-up inverter based on series-parallel conversion of switched-capacitor with the associated staircase modulation and power flow control for WPT applications. Corresponding to the system parameters of a typical electric microcars, the operating principle and the power flow control of the proposed inverter are verified by simulation. The battery power as well as the primary and secondary AC waveforms of the simulation model are presented.

Keywords–Electric vehicle (EV) charging, inductive power transfer (IPT), DC-AC power converters, switched-capacitor circuits.

I. INTRODUCTION

Wireless power transfer (WPT) is one of the emerging technologies for powering consumer electronics, portable devices and even electric vehicles (EVs). This technology greatly improves the convenience and safety, as well as enables a wide range of commercial, industrial and medical applications like electrified transportations, industrial robots, sensor networks and biomedical implants [1-9]. Inductive power transfer (IPT) is a promising and well developed technology for short to mid-range wireless applications including wireless charging for EVs. Last year, the Society of Automotive Engineers (SAE) has released the wireless charging standard, TIR J2954 [10], for light duty plug-in hybrid EVs or EVs that utilizes a common frequency band of around 80kHz to 90kHz for inductive power transfer at power levels of a few kilowatts to dozen-kilowatts. Fig. 1 illustrates a typical wireless EV charging system based on IPT [11]. The transmitter side, supplied by AC voltage source from the utility, usually consists of a power factor correction (PFC) rectifier following a high-frequency inverter to convert the output frequency and voltage level. Since the coupling factor would be very low for WPT, compensation networks would be required for both primary and secondary coils to compensate the leakage inductance which improve the power factor as well as the energy efficiency. In the receiving side, diode bridge rectifier is most commonly used to convert the high-frequency AC waveform to DC waveform and filter the voltage and current ripples with capacitor or inductor-capacitor filter.

However, the use of diode rectifier in the receiving end restricts the direction of power flow. In the conventional design, only charging operation, i.e. charging from the utility supply to the vehicle energy storage system (ESS), is permitted. This would deny the benefits provided by these grid-enable vehicles (GEVs) and sway the future implementation and development on the EV related features in smart-grid and micro-grid such as the vehicle-to-buildings (V2B) and vehicle-to-grid (V2G) applications [12]. The literature indicates that the GEVs would play a very important role in the future utility since the intelligent energy interface between the utility and the vehicles' ESSs could smooth the power pattern, support the increasing penetration of renewable energy, and even provide ancillary services to regulate the grid voltage and frequency [12-15].

The feature of bidirectional power flow could be enabled by simply substitute the diode rectifier in the receiver with inverter (Fig. 2). There are some wireless charging system designs [16-18] employing H-bridge as the pick-up converter in the receiving end for providing bidirectional power flow. However, these designs require a relative high battery voltage since the DC link voltage supplied by the PFC rectifier at the primary side could be up to several hundred-volts and the DC link voltage at the pick-up side should be in the same order of magnitude to facilitate bidirectional power flow. For small vehicles such as microcars having comparative low battery voltage, the large mismatch between the battery voltage and the DC link voltage at the charging station would increase the design and control difficulty of the charging components. For this reason, a bidirectional DC-DC converter or a step-up inverter would be required in this situation.

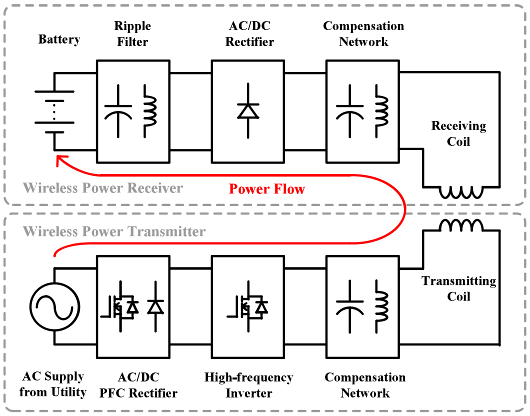

Fig. 1: A typical unidirectional wireless EV charging system based on IPT

[1, 2] Power Electronics Research Centre, Department of Electrical Engineering
The Hong Kong Polytechnic University, Hong Kong
[1]E-mail: yc-chi.fong@connect.polyu.hk

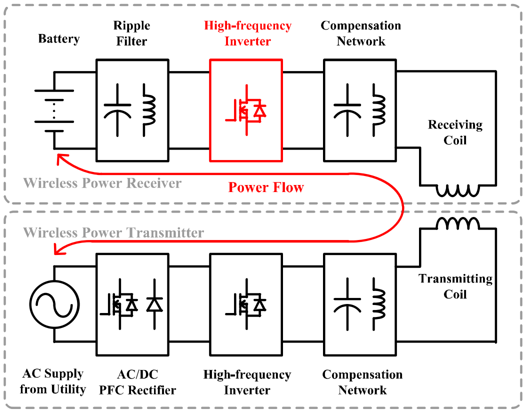

Fig. 2: A bidirectional wireless EV charging system with a high-frequency inverter in the receiver

Table I: The switching table for a 7-level SCMLI*

V_o	$C_{1a}, C_{2a}, C_{1b}, C_{2b}$	$S_{31a}, S_{32a}, S_{31b}, S_{32b}$
0	P, P, P, P	1, 0, 1, 0
V_{dc}	S, P, P, P	1, 0, 1, 0
$2V_{dc}$	S, S, P, P	1, 0, 1, 0
$3V_{dc}$	S, S, P, P	0, 1, 1, 0
$2V_{dc}$	P, S, P, P	0, 1, 1, 0
V_{dc}	P, P, P, P	0, 1, 1, 0
0	P, P, P, P	1, 0, 1, 0
$-V_{dc}$	P, P, S, P	1, 0, 1, 0
$-2V_{dc}$	P, P, S, S	1, 0, 1, 0
$-3V_{dc}$	P, P, S, S	1, 0, 0, 1
$-2V_{dc}$	P, P, P, S	1, 0, 0, 1
$-V_{dc}$	P, P, P, P	1, 0, 0, 1
0	P, P, P, P	1, 0, 1, 0

*S: Series; P: Parallel

The switched-capacitor (SC) multilevel inverter (MLI) has received more attention in recently years. This type of inverters offer voltage step-up capability and self-balancing of capacitor voltage by the technique of series-parallel conversion [19-22]. In addition, the topology presented in [19] has demonstrated the capability of SCMLI for driving inductive load; the topology suggested in [22] reduces the ratings of components by eliminating the need of H-bridge back-end. The mathematical analyses on the voltage ripples of the switched-capacitors and the energy efficiency in previous research have indicated that this type of inverters are more favorable for high-frequency applications. As the capacitor sizes are essentially inversely proportional to the operating frequency, the switched-capacitor inverters would be the ideal candidates for WPT applications working at around 80kHz.

In this paper, a SCMLI offering bidirectional power flow and voltage step-up capability, based on the principle of series-parallel conversion, is proposed for WPT applications. The operation principle of the topology as well as the modulation and power flow control will be described. The simulation of a model, based on the applications for light-duty microcars with comparatively low battery voltage, has been conducted and the corresponding results will be presented.

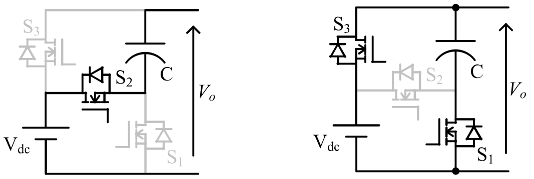

(a) (b)

Fig. 3: Series-parallel conversion of an SC cell; (a) series operation; (b) parallel operation

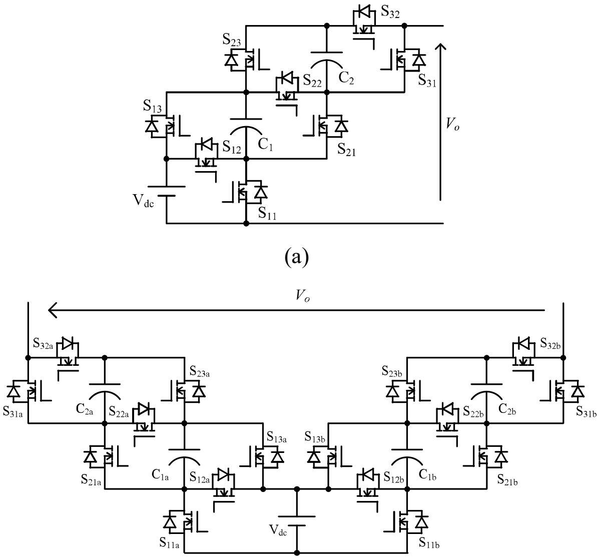

(a)

(b)

Fig. 4: The proposed switched-capacitor multilevel inverter; (a) one phase of SC converter with two SC cells; (b) a 7-level SCMLI formed by two SC converters

II. OPERATION PRINCIPLE OF THE INVERTER

1. General Description

The proposed topology is derived from the series-parallel conversion of switched-capacitor. The basic operation of an SC cell is depicted in Fig. 3. When S_1 and S_3 are conducted, the capacitor would be charged to the same voltage level as the voltage source; when only S_2 is conducted, the voltage level across the SC cell is doubled by connecting the capacitor and the voltage source in-series. One phase of SC converter, consists of two SC cells, and the proposed 7-level SCMLI, consists of two phases of SC converters, are illustrated in Fig. 4(a) and 4(b), respectively. By sequentially series and parallel switching of the SC cells, multilevel voltage waveforms could be produced at the output terminal of an SC converter phase; by applying time (phase angle) shift between two phases, bipolar multilevel voltage waveforms are produced across the terminals of different phases. As the switches for both series and parallel operations allow current flow of both directions at on-state, the capacitors could be charged by both DC bus and AC bus. Therefore, the proposed SCMLI topology is capable of handling power flow in both directions.

In the proposed topology, bipolar output voltage waveforms are produced by the phase angle difference

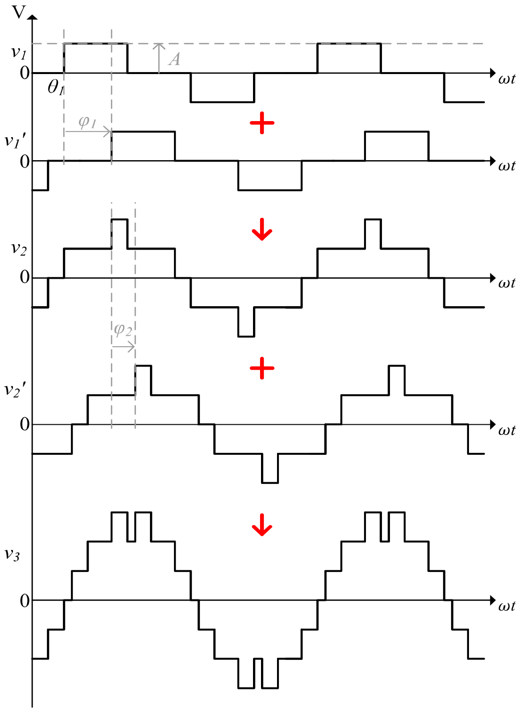

Fig. 5: Synthesis of 7-level staircase voltage waveform based on phase-shift and superposition

between the SC converters. In each of the SC converters, the voltage stresses of the active switches are limited by the operating voltage of the SC cells, which is about the same magnitude as the DC bus. By eliminating the need of the high voltage H-bridge, the maximum voltage ratings of the semiconductor switches are greatly reduced comparing to the designs suggested in [19-21]. A table of switching states for different output voltage level for a 7-level inverter is listed in table I. The operation of the proposed topology is time interleaved by adopting the multiphase structure. A much longer parallel duration for capacitor charging is provided, therefore, a significantly higher maximum operating frequency would be allowed, compared to the existing SCMLIs suggested in [19-22].

2. Staircase Modulation with Phase-shift Harmonic Elimination Technique

Considering that the switching losses of the inverter are roughly proportional to the switching frequency, the switching losses would be too high if high frequency modulation method like the level-shifted or phase-shifted PWM is employed. For the high-frequency applications such as WPT, staircase modulation methods working at the fundamental output frequency are preferred. As shown in Fig. 2, the IPT system consists of compensation networks in both primary and secondary sides. The compensation networks could form band-pass filters with the self or leakage inductance of the transmitting or receiving coils. When operating near the resonant frequency, the roll-off of the band-pass filters would be fast enough to filter most of the high-frequency harmonic contents.

Selective harmonic elimination (SHE) [23] is one of the most common fundamental frequency modulation techniques for multilevel inverter. The SHE technique computes the firing angles for a specific modulation index and eliminating the selected harmonic contents, usually the lowest order harmonics, by solving a system of nonlinear equations. SHE is effective generating the required staircase voltage waveforms which precisely preserves the amplitude of fundamental component and rejects the low order harmonics, yet the conventional SHE method demands a lot of computation which is time consuming and difficult to be implemented in real-time [24-25]. Instead of solving a system of nonlinear equations, a simpler phase-shift technique is employed in this study to compute the firing angles.

Fig. 5 explains the synthesis of 7-level staircase voltage waveform based on the phase-shift harmonic elimination technique. v_1 represents the one-step voltage waveform and v_1' is the phase-shifted waveform of v_1. v_2 is the two-step voltage waveform synthesized by superposing v_1 and v_1'. Similarly, v_2' is the phase-shifted waveform of v_2; v_3 is synthesized from v_2 and v_2'. If the firing angle of v_1 is θ_1, based on Fourier analysis, the amplitudes of the fundamental voltage as well as the harmonics would be

$$A_{1,n} = \frac{4A}{n\pi}\cos(n\theta_1) \tag{1}$$

where $n = 1, 3, 5, \ldots$, is the harmonic order ($n = 1$ represents the fundamental component). By phase-shifting v_1 by φ_1 and superposing to itself, the Fourier coefficients of the resultant waveform v_2, would be

$$A_{2,n} = \frac{8A}{n\pi}\cos(n\theta_1)\sin\left(\frac{\pi + n\varphi_1}{2}\right) \tag{2}$$

Similarly, by phase-shifting v_2 by φ_1 and superposing them again, the decomposed amplitudes of v_3 would be

$$A_{3,n} = \frac{16A}{n\pi}\cos(n\theta_1)\sin\left(\frac{\pi + n\varphi_1}{2}\right)\sin\left(\frac{\pi + n\varphi_2}{2}\right) \tag{3}$$

By means of putting the specific harmonics to zero, i.e.

$$\begin{cases} \sin\left(\dfrac{\pi + n_1\varphi_1}{2}\right) = 0 \\ \sin\left(\dfrac{\pi + n_2\varphi_2}{2}\right) = 0 \end{cases} \tag{4}$$

the corresponding harmonic contents could be eliminated easily. The fundamental amplitude of the resultant waveform, v_3, could be expressed as (5).

$$A_{3,1} = \frac{16A}{\pi}\cos(\theta_1)\sin\left(\frac{\pi + \varphi_1}{2}\right)\sin\left(\frac{\pi + \varphi_2}{2}\right) \tag{5}$$

By definition, the modulation index, m, for the 7-level MLI is

$$m = \frac{\pi A_{3,1}}{12 V_{dc}} \tag{6}$$

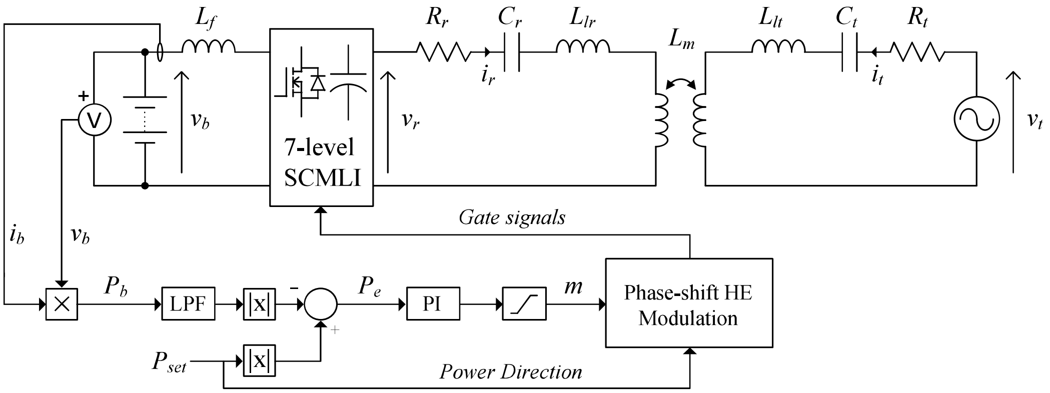

Fig. 7: Schematic for the configuration of the simulation model

By putting (5) into (6), the modulation index of the 7-level inverter could be a function of θ_1, φ_1 and φ_2, i.e.

$$m = \frac{4}{3}\cos(\theta_1)\sin\left(\frac{\pi+\varphi_1}{2}\right)\sin\left(\frac{\pi+\varphi_2}{2}\right) \tag{7}$$

As φ_1 and φ_2 would be constant values for eliminating predefined harmonics, the sine terms could be calculated offline. Thus, the modulation index of the inverter could be controlled by the firing angle, θ_1, easily.

Since v_3 is synthesized by superposing two two-step voltage waveforms, the maximum number of steps would be four. In order to limit the maximum number of steps of v_3 to three, the following criteria should be fulfilled.

$$\begin{aligned} \theta_1 + \varphi_1 + \varphi_2 &> \pi - \theta_1 \\ \theta_1 &> \frac{\pi - \varphi_1 - \varphi_2}{2} \end{aligned} \tag{8}$$

Therefore, the maximum modulation index for the 7-level MLI, which eliminates two sets of harmonics by the phase-shift harmonic elimination technique, would be limited such that

$$m < \frac{4}{3}\cos\left(\frac{\pi-\varphi_1-\varphi_2}{2}\right)\sin\left(\frac{\pi+\varphi_1}{2}\right)\sin\left(\frac{\pi+\varphi_2}{2}\right) \tag{9}$$

For example, if the 3rd, 9th,… and 5th, 15th,… harmonics are eliminated, the maximum attainable modulation index, m_{max}, would be

$$\begin{aligned} m_{\max} &= \frac{4}{3}\cos\left(\frac{7\pi}{30}\right)\sin\left(\frac{2\pi}{3}\right)\sin\left(\frac{3\pi}{5}\right) \\ &\approx 0.8161 \end{aligned} \tag{10}$$

3. Power Flow Control

LC-series structure is one of the most basic compensation configurations for IPT systems. The equivalent circuit for a series-series compensation network is depicted in Fig. 6. v_p and v_s are the output voltage of the inverters at primary side and secondary side, respective. C_p, R_p, C_s, and R_s are the compensation capacitances and the equivalent series resistance for the primary and secondary coils. L_{lp}, L_{ls} and L_m are the primary leakage inductance, secondary leakage inductance and mutual inductance of the transmission coils, i.e. $L_p = L_{lp} + L_m$ and $L_s = L_{ls} + L_m$.

The real and reactive power from the primary side could be evaluated by the following

$$\begin{cases} P = \mathrm{Re}(v_p i_p^*) \\ Q = \mathrm{Im}(v_p i_p^*) \end{cases} \tag{11}$$

If the self-inductance of the primary and secondary coils are compensated at the same resonant frequency and both the primary and secondary inverters operate at the resonant frequency, i.e.

$$\omega = \frac{1}{\sqrt{L_p C_p}} = \frac{1}{\sqrt{L_s C_s}} \tag{12}$$

The input power at the primary side could be derived as the following [26]

$$\begin{cases} P = \dfrac{V_p V_s}{2L_m\omega}\sin\delta \\ Q = \dfrac{V_p V_s}{2L_m\omega}\cos\delta \end{cases} \tag{13}$$

where, V_p and V_s are the fundamental amplitudes of the primary and secondary voltages, and δ is the phase angle difference. Referring to (13) the magnitudes of the real and reactive power could be controlled by the modulation index, while the power factor as well as the direction of power flow could be controlled by the phase-shift. Also, the maximum power factor and efficiency would be attained when the phase-shift is $\pm\pi/2$.

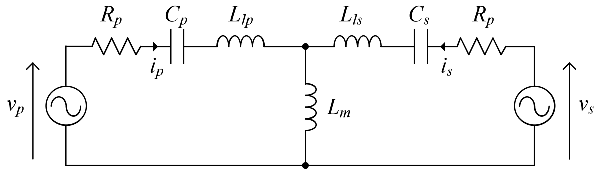

Fig. 6: The equivalent circuit for IPT with series-series LC compensation network

Table II: Parameters of the simulation model

Parameter	Value
Battery voltage (V_b)	120V
Secondary AC source	400V_{peak}
Filter inductor (L_f)	10µH, 10mΩ
Switched-capacitors	10µF, 50mΩ
MOSFET $R_{ds(on)}$	50mΩ
R_1, R_2	1.5Ω
C_1, C_2	20nF
L_{l1}, L_{l2}	144µH
L_m	36µH
Operating frequency	84kHz

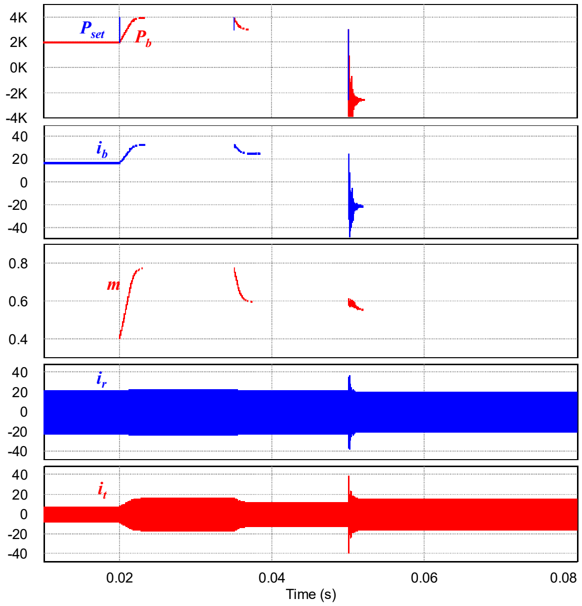

Fig. 8: Simulated waveforms of the models; the battery power, P_b, and power set-point, P_{set}; battery current, i_b; modulation index, m; current of the primary and secondary coils, i_r and i_t

III. VERIFICATIONS

In order to verify the operation of the proposed topology, a simulation model of an IPT system, employing the 7-level SCMLI at one side, was implemented. The magnitude of the real power was controlled by PI compensation; the battery power was calculated form the instantaneous battery voltage and current, and the calculated power was compared with the power set-point; the error was inputted to the PI controller which generated the required modulation index. The direction of power flow was determined by the phase angle, which could be either π/2 or –π/2. Fig. 7 illustrates the simulation set-up; the associated parameters are shown in table II.

In the simulation model, the battery voltage, v_b, was 120V. The voltage was stepped-up and inverted by the 7-level SCMLI, the capacitance of each of the switched-capacitor was 10µF. The power was transmitted through the inductive coils with self-inductance of 180µH which were compensated by series capacitors. In the secondary side, an AC voltage source of 400V peak voltage was used to simulate the inverter output at the charging pad. The operating frequency of the simulated IPT system was 84kHz such that the compensation capacitance was resonated with the self-inductance of the coils. The simulated waveforms are illustrated in Fig. 8. At the beginning, the power set-point for the battery was 2000W, then, it was doubled at $t = 0.02s$; and then declined to 3000W at $t = 0.035s$. At $t = 0.05s$, the battery was altered to charging mode by setting the power to −2000W. As shown in the results, the simulated battery power would able to track the set-point value and control the power flow with the aforementioned technique. In addition, a few cycles of power oscillating was observed at the instant of change in direction. It was due to the fact that the phase change was applied during non-zero current. This issue could be improved if the controller could apply the π-shift at zero-current by zero-crossing detection and soft-altering. Furthermore, the inverter output waveforms at around $t = 0.03s$, generated by the phase-shift harmonic elimination technique are illustrated in Fig. 9. From the corresponding fast Fourier transform (FFT) shown in Fig. 10, it could be observed that the 3rd, 9th,… and 5th, 15th,…, voltage harmonics were removed; and most of the remaining harmonics were effectively filtered by the resonant circuit. At P_b = 4000W, the voltage ripples of the capacitors was only about 8% of the charging voltage, this suggested that the proposed SCMLI with the above-mentioned parameters would be capable of WPT applications at a few kilowatts.

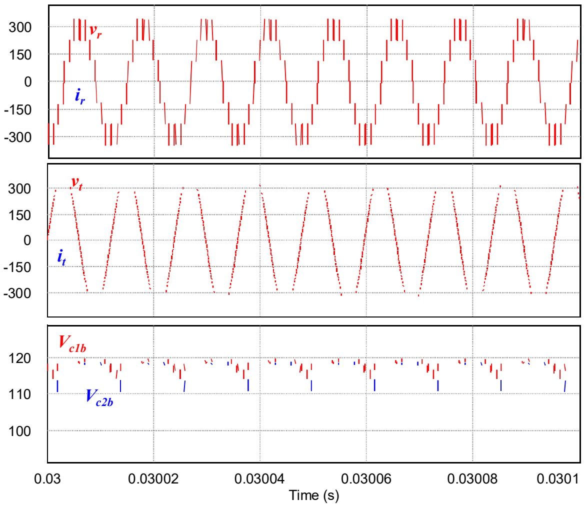

Fig. 9: The AC waveforms and the corresponding switched-capacitor voltage at around t = 0.03s; the output voltage, v_r, and current, i_r, of the 7-level SCMLI; the secondary coil current, i_t, and AC source voltage, v_t; the voltage of the switched-capacitor C_{1b} and C_{2b}

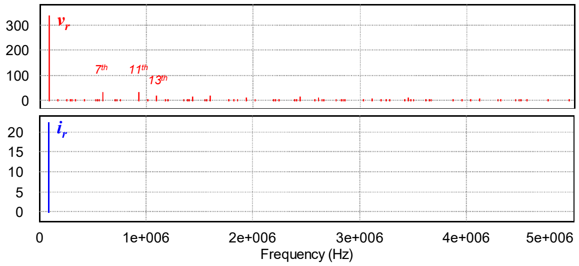

Fig. 10: Fast Fourier transform (FFT) of the output voltage, v_r, and current, i_r, of the 7-level SCMLI

IV. CONCLUSION

A high-frequency inverter for WPT applications based on the series-parallel conversion technique is presented. The voltage step-up feature improves the capability of bidirectional power flow without the need of DC-DC converter stage in small vehicles having relative low battery voltage like microcars. The presented modulation and control techniques are easily to implement and effective for high-frequency applications like IPT. With the built-in resonant tanks, the inverter could achieve satisfactory power quality with simple harmonic elimination technique. The topology as well as the operation principles of the proposed inverter was verified by simulation. Comparing to the conductive applications, the SCMLI is capable of higher power level at small capacitor sizes due to the substantial increase in frequency.

ACKNOWLEDGMENT

The authors wish to acknowledge the support provided by the members of the Power Electronics Research Centre (PERC) and Research Committee at The Hong Kong Polytechnic University.

REFERENCES

[1] A. Kawamura, K. Ishioka and J. Hirai, "Wireless transmission of power and information through one high-frequency resonant AC link inverter for robot manipulator applications," in *IEEE Trans. on Ind. Appl.*, vol. 32, no. 3, pp. 503-508, May/Jun 1996.

[2] K. O'Brien, G. Scheible and H. Gueldner, "Analysis of wireless power supplies for industrial automation systems," *Ind. Electron. Society, 2003. IECON '03. The 29th Annual Conf. of the IEEE*, 2003, pp. 367-372 vol.1.

[3] S. Y. R. Hui and W. W. C. Ho, "A new generation of universal contactless Battery Charging platform for portable Consumer Electronic equipment," in *IEEE Trans. on Power Electron.*, vol. 20, no. 3, pp. 620-627, May 2005.

[4] C. H. Hu, C. M. Chen, Y. S. Shiao, T. J. Chan and T. R. Chen, "Development of a universal contactless charger for handheld devices," *2008 IEEE Int. Symp. on Ind. Electron.*, Cambridge, 2008, pp. 99-104.

[5] G. A. Covic and J. T. Boys, "Modern Trends in Inductive Power Transfer for Transportation Applications," in *IEEE Journal of Emerging and Selected Topics in Power Electron.*, vol. 1, no. 1, pp. 28-41, March 2013.

[6] O. C. Onar, J. M. Miller, S. L. Campbell, C. Coomer, C. P. White and L. E. Seiber, "A novel wireless power transfer for in-motion EV/PHEV charging," *2013 Twenty-Eighth Annual IEEE Applied Power Electron. Conf. and Exposition (APEC)*, Long Beach, CA, USA, 2013, pp. 3073-3080.

[7] Q. Xu, H. Wang, Z. Gao, Z. H. Mao, J. He and M. Sun, "A Novel Mat-Based System for Position-Varying Wireless Power Transfer to Biomedical Implants," in *IEEE Trans. on Magnetics*, vol. 49, no. 8, pp. 4774-4779, Aug. 2013.

[8] M. Erol-Kantarci and H. T. Mouftah, "Suresense: sustainable wireless rechargeable sensor networks for the smart grid," in *IEEE Wireless Communications*, vol. 19, no. 3, pp. 30-36, June 2012.

[9] G. Covic and J. Boys, “Inductive power transfer,” *Proc. IEEE*, vol. 101, no. 6, pp. 1276–1289, Jun. 2013.

[10] (2017). [Online]. Available: standards.sae.org/wip/j2954/

[11] B. Esteban, M. Sid-Ahmed and N. C. Kar, "A Comparative Study of Power Supply Architectures in Wireless EV Charging Systems," in *IEEE Trans. on Power Electron.*, vol. 30, no. 11, pp. 6408-6422, Nov. 2015.

[12] A. G. Boulanger, A. C. Chu, S. Maxx and D. L. Waltz, "Vehicle Electrification: Status and Issues," in *Proc. of the IEEE*, vol. 99, no. 6, pp. 1116-1138, June 2011.

[13] W. Su, H. Eichi, W. Zeng and M. Y. Chow, "A Survey on the Electrification of Transportation in a Smart Grid Environment," in *IEEE Trans. on Ind. Informatics*, vol. 8, no. 1, pp. 1-10, Feb. 2012.

[14] H. N. T. Nguyen, C. Zhang and M. A. Mahmud, "Optimal Coordination of G2V and V2G to Support Power Grids With High Penetration of Renewable Energy," in *IEEE Trans. on Transportation Electrification*, vol. 1, no. 2, pp. 188-195, Aug. 2015.

[15] Y. He, B. Venkatesh and L. Guan, "Optimal Scheduling for Charging and Discharging of Electric Vehicles," in *IEEE Trans. on Smart Grid*, vol. 3, no. 3, pp. 1095-1105, Sept. 2012.

[16] J. Y. Lee and B. M. Han, "A Bidirectional Wireless Power Transfer EV Charger Using Self-Resonant PWM," in *IEEE Trans. on Power Electron.*, vol. 30, no. 4, pp. 1784-1787, April 2015.

[17] L. Zhao, D. J. Thrimawithana and U. K. Madawala, "Hybrid Bidirectional Wireless EV Charging System Tolerant to Pad Misalignment," in *IEEE Trans. on Ind. Electron.*, vol. 64, no. 9, pp. 7079-7086, Sept. 2017.

[18] A. A. S. Mohamed, A. Berzoy, F. G. N. de Almeida and O. Mohammed, "Modeling and Assessment Analysis of Various Compensation Topologies in Bidirectional IWPT System for EV Applications," in *IEEE Trans. on Ind. Appl.*, vol. 53, no. 5, pp. 4973-4984, Sept.-Oct. 2017.

[19] Y. Hinago and H. Koizumi, "A Switched-Capacitor Inverter Using Series/Parallel Conversion With Inductive Load," in *IEEE Trans. on Ind. Electron.*, vol. 59, no. 2, pp. 878-887, Feb. 2012.

[20] Y. Ye, K. W. E. Cheng, J. Liu and K. Ding, "A Step-Up Switched-Capacitor Multilevel Inverter With Self-Voltage Balancing," in *IEEE Trans. on Ind. Electron.*, vol. 61, no. 12, pp. 6672-6680, Dec. 2014.

[21] E. Zamiri, N. Vosoughi, S. H. Hosseini, R. Barzegarkhoo and M. Sabahi, "A New Cascaded Switched-Capacitor Multilevel Inverter Based on Improved Series–Parallel Conversion With Less Number of Components," in *IEEE Trans. on Ind. Electron.*, vol. 63, no. 6, pp. 3582-3594, June 2016.

[22] Y. C. Fong, S. Raghu Raman, M. Moonson Chen and K.W.E. Cheng, "A Novel Switched-capacitor Multilevel Inverter Offering Modularity in Design," 2018 *IEEE Applied Power Electron. Conf. and Exposition (APEC)*, San Antonio, TX, 2018.

[23] J. R. Wells, B. M. Nee, P. L. Chapman and P. T. Krein, "Selective harmonic control: a general problem formulation and selected solutions," in *IEEE Trans. on Power Electron.*, vol. 20, no. 6, pp. 1337-1345, Nov. 2005.

[24] D. Ahmadi, K. Zou, C. Li, Y. Huang and J. Wang, "A Universal Selective Harmonic Elimination Method for High-Power Inverters," in *IEEE Trans. on Power Electron.*, vol. 26, no. 10, pp. 2743-2752, Oct. 2011.

[25] M. Ahmed, A. Sheir and M. Orabi, "Real-Time Solution and Implementation of Selective Harmonic Elimination of Seven-Level Multilevel Inverter," in *IEEE Journal of Emerging and Selected Topics in Power Electron.*, vol. 5, no. 4, pp. 1700-1709, Dec. 2017.

[26] A. A. S. Mohamed, A. Berzoy, F. G. N. de Almeida and O. Mohammed, "Modeling and Assessment Analysis of Various Compensation Topologies in Bidirectional IWPT System for EV Applications," in *IEEE Trans. on Ind. Appl.*, vol. 53, no. 5, pp. 4973-4984, Sept.-Oct. 2017.

Asian Power Electronics Journal, Vol. 13 , No.1, June 2019

A Novel Hybrid-Excited Flux-Modulated Memory Machine for Electrical Continuously Variable Transmission System

Mao Y [1] Niu S. X [2]

Abstract–This paper proposed a hybrid-excited double rotor double stator permanent magnetic machine applied in electrical continuously variable transmission (E-CVT) system which incorporates with the flux modulation and flux-memorizable concept. This machine can produce relative large torque in low speed region owing to flux modulation effect. Besides, this E-CVT system can achieve high speed operation in flux weakening mode which is realized by applying a short current pulse to demagnetize aluminum-nickel-cobalt (AlNiCo) magnets in this machine. There is no need to introduce a permanent excitation current in winding for this machine which results in avoiding inducing additional excitation losses. The configuration and operation principles of the proposed hybrid-excited flux-modulated memory (HEFMM) machine are presented. Electromagnetic characteristics of the proposed machine are analyzed using the time-stepping finite element method (TS-FEM).

Keywords–Electrical continuously variable transmission system, finite element method, flux modulation, memory machine

I. INTRODUCTION

With continuous growth in the number of hybrid electric vehicles (HEV), the request to improve its fuel economy and energy efficiency is increasing accordingly. Electrical continuously variable transmission (E-CVT) system is a desired technology to fulfill these requirements which can realize combination and separation of the power provided by both internal combustion engine (ICE) and the energy storage system [1]-[5].

The Toyota Prius E-CVT system which consists of a planetary gear power slit system and two electric machines with associated power inverters is a milestone in the development of HEVs [6]. In this E-CVT system, there is a planet gear connected with ICE, of which the sun gear is connected with the electric machine and the ring gear is connected to the other electric machine. This design effectively provides a fully integrated power supply system to realize acquisition, storage and conversion of energy. However, this E-CVT system integrated with mechanical planetary gearbox system suffers from relatively low reliability and low efficiency. Therefore, gearless E-CVT systems adopt permanent magnetic (PM) gears are gradually developed to replace conventional E-CVT systems employed mechanical gears [7]–[11]. Among these designs, permanent magnetic (PM) machines as well as induction machines with double rotor constructions can nicely split and combine power without plagued by mechanical problems such as frictional loss, high maintenance and audible noise various. In[9] a double stator double rotor brushless ECVT system is proposed. The core component of this E-CVT system includes a double-stator double-rotor flux-modulated machine and an energy storage system combined with several inverters . The schematic diagram of this E-CVT system is plotted as shown in Fig.1. The two rotors in this E-CVT system are coupled due to flux modulation effect. Compared to other designs, this kind of E-CVT system has many merits such as high torque density, high efficiency, integrated structure and low mutual effect between each winding [12-13]. But since the drive's output voltage is limited by its dc bus, this E-CVT system may not realize the requirement in driving speed. Due to the fixed magnetic field of PM excitation, it is difficult for this machine to regulate magnetic flux so that not easy to accommodate HEV to different drive mode. So in this paper, a novel hybrid-excited flux-modulated memory (HEFMM) machine for E-CVT system is proposed to address these problems. The configuration of the core component of the proposed E-CVT system is shown in Fig. 2. Operation principles of the proposed E-CVT system are described in section II and performance of the HEFMM machine based on time-stepping finite element method (TS-FEM) are reported in section III.

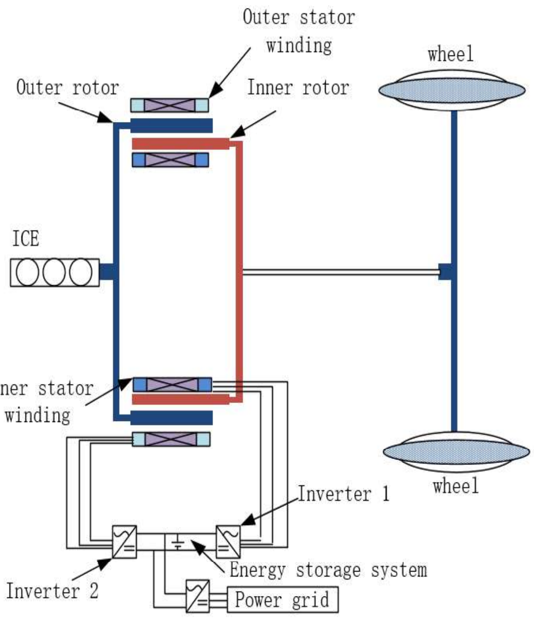

Fig. 1: Schematic diagram of the double rotor double stator ECVT system

II. CONFIGURATION AND OPERATION PRINCIPLE OF THE HYBRID-EXCITATION MACHINE

The cross section configuration of the machine part of the E-CVT system is shown in Fig.2. This machine is

---

[1] Department of Electrical Engineering, The Hong Kong Polytechnic University, Hong Kong
E-mail: yuan.my.mao@polyu.connect.hk
[2] Department of Electrical Engineering, The Hong Kong Polytechnic University, Hong Kong
E-mail: eesxniu@polyu.edu.hk

composed of two stators, two rotors and three sets of windings. Both the inner stator and the outer stator are housed with a set of armature winding. In addition, another set of windings is introduced to the inner stator which is used to bear excitation current pulse. In this design, the aluminum-nickel-cobalt (AlNiCo) magnet segments and ferrite segments are attached to each tooth of the inner stator one by one. The magnetization coils are wound around the teeth behind the AlNiCo pieces. By applying a temporary current pulse to each coils, the AlNiCo magnets can be either magnetized or demagnetized [14-15]. With this design, the level of air gap flux density can be effectively regulated. The inner rotor and outer rotor in this machine both adopt surface mounted structure with the arrangement of one-PM-one-ferrite. The rotor PM material is NdFeB which is magnetized in radically outward direction in both two rotors.

.

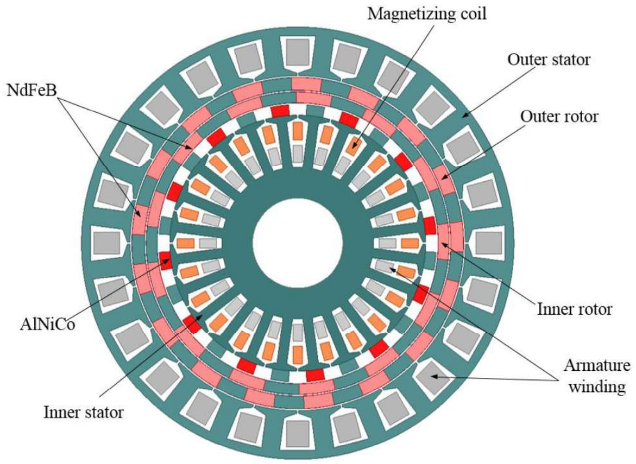

Fig. 2: Configuration of the hybrid-excited flux-modulated memory (HEFMM) machine for E-CVT system.

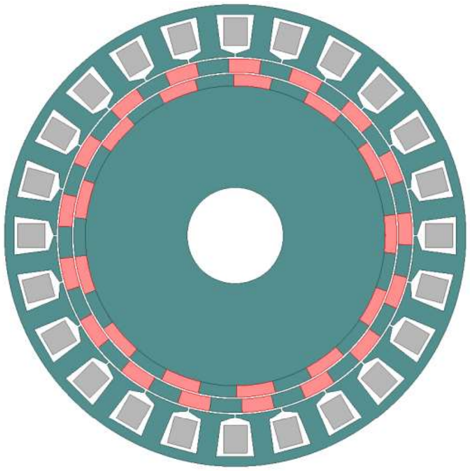

(a)

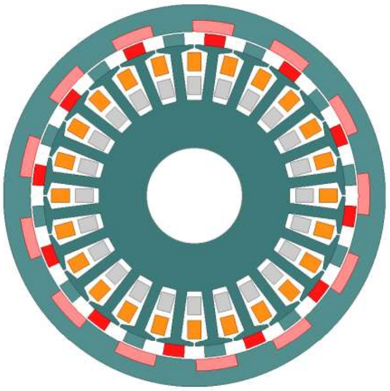

(b)

Fig. 3: The cross section configuration of equivalent part of the proposed HEFMM machine for E-CVT system: (a) MGM (b) MFMMM .

The structure of the proposed HEFMM machine can be seen as an integration of a magnetic gear machine (MGM) and a flux-modulated mnemonic machine (FMMM). As shown in Fig.3(a), the inner rotor, outer rotor and outer stator compose the MGM. Fig.3 (b) exhibits the configuration of FMMM which consists of the inner stator with AlNiCo flux modulator and the inner rotor.

The outer stator winding of the MGM in this design will interact with both inner and outer rotor. The operation principle of the MGM is based on the “magnetic gearing effect” which is governed by the following equation [16]:

$$P_{so}=N_{ro}-N_{ri} \tag{1}$$

where; N_{ri} and N_{ro} is the number of PM poles of the inner rotor and outer rotor respectively. P_{so} is the pole-pair number of the armature winding of outer stator. In this design, N_{ri}, N_{ro} and P_{so} are designed as 13, 17 and 4 respectively. Assuming the rotating speed of inner rotor and outer rotor are ω_{ri} and ω_{ro} respectively, the rotating speed of the outer stator winding field is ω_{so}, the rotational speeds and pole-pair number of two rotors and outer stator winding should satisfy the following equation:

$$-N_{ri}\omega_{ri}+N_{ro}\omega_{ro}+P_{so}\omega_{so}=0 \tag{2}$$

From (1) and (2) the rotating speed of armature winding field in outer stator can be expressed as:

$$\omega_{so}=\frac{N_{ri}\omega_{ri}-N_{ro}\omega_{ro}}{N_{ri}-N_{ro}}=\frac{N_{ri}\omega_{ri}-N_{ro}\omega_{ro}}{P_{so}} \tag{3}$$

So the frequency of armature current of outer stator winding is:

$$f_{so}=\frac{N_{ri}\omega_{ri}-N_{ro}\omega_{ro}}{60} \tag{4}$$

The FMMM part of the proposed HEFMM machine includes the inner stator and the mnemonic magnet modulator which can nicely interact with the inner rotor. The pole pair number of the inner rotor N_{ri}, the pole pair number of the modulator N_m and the pole pair number of the armature winding field of inner stator P_{si} also satisfy the principle of magnetic gear effect and governed by the equation[16]:

$$P_{si}=N_{ri}-N_m \tag{5}$$

In order to couple with design of the MGM part, N_m and P_{si} are set as 12 and 1 respectively. In the same way, the rotating speed of armature winding field in inner stator match the following formula:

$$\omega_{si}=\frac{N_{ri}\omega_{ri}}{N_{ri}-N_m}=\frac{N_{ri}\omega_{ri}}{P_{si}} \tag{6}$$

Accordingly, the frequency of inner stator armature winding can be given as:

$$f_{si}=\frac{N_{ri}\omega_{ri}}{60} \tag{7}$$

Only when rotating speed of inner rotor and outer rotor match the frequency of armature winding field of inner stator and outer stator, the machine can work well to transmit steady torque. The specifications of the double rotor double stator hybrid-excitation machine in E-CVT system are listed in Table I. Due to flux modulation effect, when the inner rotor rotates at certain speed, field harmonics in the airgap are generated. Thus the rotors and the stator armature winding can interact with each other via common harmonics components. More specially, for the proposed MFMM in this paper, the 1-pole-pair main flux with the 13-pole-pair harmonic component exists in the inner airgap. On the other hand, in the outer airgap, there is the 13-pole-pair main flux with the 1-pole-pair harmonic component. The inner stator teeth employed with AlNiCo magnet and ferromagnetic poles work as a modulator to transform pole pairs between inner and outer airgaps. The 13-pole-pair flux excited by NdFeB magnet sets becomes 1-pole-pair in the inner airgap due to the modulation effect of the AlNiCo magnet or ferromagnetic pole-pieces.

As shown in Fig.4, the NdFeB magnet pieces embedded in inner rotor and outer rotor are all magnetized radially outwards. Since AlNiCo magnet material has intrinsically low coercivity and high remanence, its magnetization level can be adjusted by applying a temporary current pulse to the magnetizing coil housed in the inner stator. On the other hand, the coercivity of NdFeB magnet material is too high to be changed by this small current pulse. When the AlNiCo magnet pieces are magnetized to the same magnetization direction with the NdFeB magnet pieces, the magnetic fluxes are enforced. When the AlNiCo magnet pieces are demagnetized to the opposite magnetization direction, the magnetic flux with the NdFeB magnet pieces will produce a flux leakage loop via the AlNiCo magnet pieces and not link with the inner stator armature winding [17].

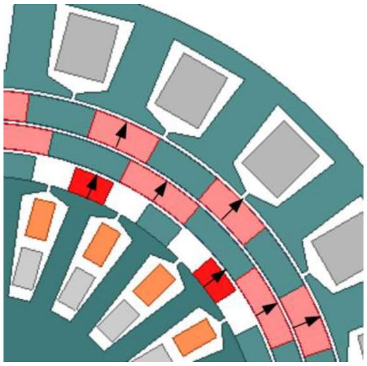
(a)

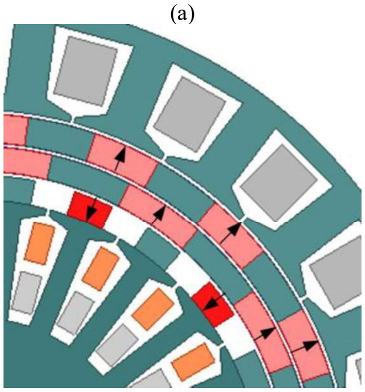
(b)

Fig. 4: Schematic diagram of the magnetization direction under (a) magnetization level (b) demagnetization level of the HEFMM machine.

Table 1: Specifications of the Double Rotor Double Stator Hybrid-excitation Machine In ECVT System

Symbol	Description	Unit	Value
D	Outer diameter	mm	240
l	Stack length	mm	65
h_{ri}	thickness of inner rotor	mm	6
h_{ro}	thickness of outer rotor	mm	7
h_m	thickness of AlNiCo pieces	mm	6
P_{so}	pole pair number of outer stator armature winding	N/A	4
P_{si}	pole pair number of outer stator armature winding	N/A	1
N_{ro}	pole pair number of outer rotor	N/A	17
N_{ri}	pole pair number of inner rotor	N/A	13
ω_{ro}	rotating speed of outer rotor	rpm	-150
ω_{ri}	rotating speed of inner rotor	rpm	300
a	air gap length	mm	1
$N1$	coil turns of outer stator winding	N/A	50
$N2$	coil turns of inner stator winding	N/A	50
Z	phase number	N/A	3

III. APPLICATION APPROACH AND PERFORMANCE ANALYSIS

In contrast to fuel vehicles and battery electric vehicles (BEVs), HEVs should adapt to different drive mode by means of E-CVT systems [18]. In this design the inner

MFMMM serve as the primary motor with its rotor connected to the drive line while the outer DVPM machine serve as an auxiliary motor that connected to the internal combustion engine (ICE). When the HEV needs more power in climbing or starting up mode, the ICE will run and drive the auxiliary motor. On the other hand, when the HEV is driven at regenerative braking, idling time or downhills, the redundant energy provided by the wheels can be transformed into electrical energy and stored in the battery or ultracapacitor. By controlling the DC current pulse in the magnetization winding, the back emf can be reduced which allows more extensive speed range of the drive line. In a word, this E-CVT system can keep the HEV driven in a smooth and wide range speed under different drive mode.

The electromagnetic characteristics of the proposed machine are analyzed using TS-FEM. Compared with ac vector control in a traditional PM machine, the flux control of the proposed MFMMM is much simple. Only the direction of the DC current pulse in magnetization coils need to be controlled to demagnetize or magnetize AlNiCo magnet. Fig. 5 expresses the no-load magnetic field distribution of the proposed HEFMM machine under different magnetization level. It can be seen that magnetic field intensity of the proposed machine in magnetization level are much higher than that in demagnetization level. Corresponding back emf waveforms of inner stator winding and outer stator winding are shown in Fig.6. It clearly demonstrates that the amplitude of back emf of inner stator winding decreases from 50V to 30V after demagnetization. While, the outer stator winding's emf waveforms stay unchanged after magnetize and demagnetize process of AlNiCo magnet modulator. The torque waveforms of inner rotor and outer rotor are shown in Fig.7. The report shows that inner rotor torque can be regulated.

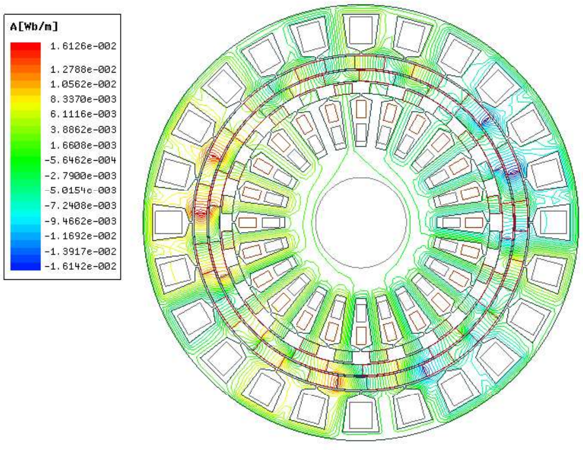

(a)

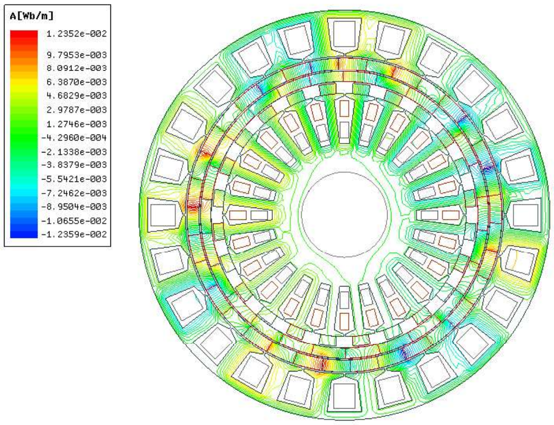

(b)

Fig. 5: No-load magnetic field distribution of the proposed HEFMM machine under (a) magnetization level (b) demagnetization level.

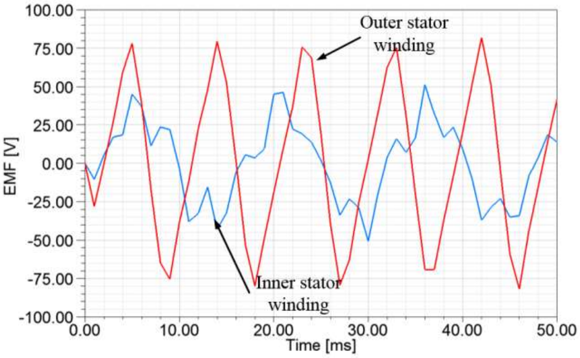

(a)

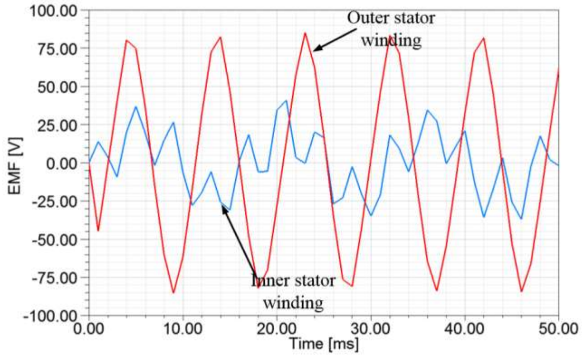

(b)

Fig. 6: No-load back emf waveforms of inner stator and outer stator of the proposed double rotor double stator machine under (a) magnetization level (b) demagnetization level.

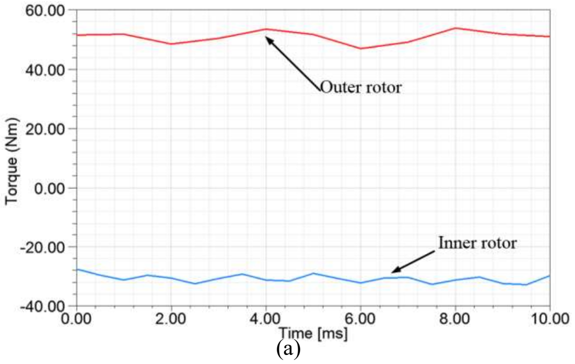

(a)

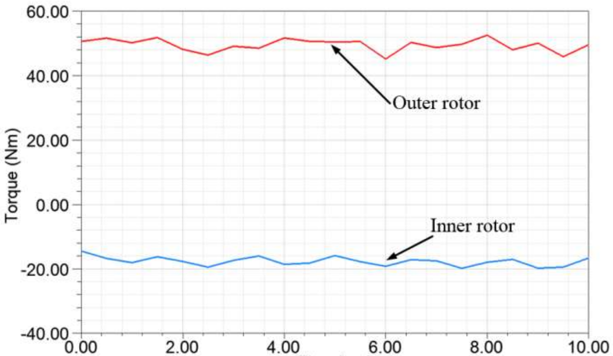

(b)

Fig. 7: Torque waveforms of the poposed HEFMM machine under (a) magnetization level (b) demagnetization level.

IV. CONCLUSION

In a HEV, the E-CVT system is the core technology that converts the kinetic energy to the electric energy, and vise versa. A gearless E-CVT system which offer higher torque density, better stability and lower friction loss usually includes a PM machine, some inverters and a battery or ultracapacitor. But due to the drive’s output voltage is limited by its dc bus, the E-CVT system may not realize the requirement in driving speed. To solve these problems, this paper proposed a novel double rotor double stator hybrid-excitation machine employing flux-modulated mnemonic design. Analysis based on TS-FEM has been conducted and the results are reported The simulation results validate the effectiveness of the proposed HEFMM machine.

ACKNOWLEDGMENT

This work was supported by research grants (Project 4-ZZBM and PolyU 152130/14E) of the Research Grants Council in the Hong Kong Special Administrative Region, China.

REFERENCES

[1] Y. Wang, M. Cheng, and K. T. Chau, “Review of electronic-continously variable transmission propulsion system for full hybrid electric vehicles,” *J. Asian Electr. Veh.*, vol. 7, no. 2, Dec. 2009.

[2] Qingsong Wang, S. Niu, X. Luo, “A Novel Hybrid Dual-PM Machine Excited by AC With DC Bias for Electric Vehicle Propulsion,” *IEEE Transactions on Industrial Electronics*, vol. 64, No. 9, Sept. 2017, pp. 6908 - 6919.

[3] Qingsong Wang, Shuangxia Niu, “A Novel Hybrid-Excited Flux Bidirectional Modulated Machine for Electric Vehicle Propulsion,” *Vehicle Power and Propulsion Conference (VPPC), 2016 IEEE.*

[4] Y. Mao, S. Niu, Y. Yang, “Differential Evolution Based Multi-Objective Optimization of the Electrical Continuously Variable Transmission System,” *IEEE Transactions on Industrial Electronics* ,2017.

[5] Yulong Liu, Shuangxia Niu, Weinong Fu, “Design of an Electrical Continuously Variable Transmission Based Wind Energy Conversion System,” *IEEE Transactions on Industrial Electronics, v*ol.63, No.11, Nov. 2016, pp. 6745 - 6755.

[6]S. Sasaki, “Toyota’s newly developed hybrid powertrain,” in *Proc. IEEE Int. Symp. Power Semiconductor Devices and ICs*, 1997, pp. 17-22.

[7]S. Niu, S. L. Ho, and W. N. Fu, “Design of a novel electrical continuously variable transmission system based on harmonic spectra analysis of magnetic field,” *IEEE Trans. Magn.*, vol. 49, no. 5, pp. 2161 – 2164, May. 2013.

[8]Y. Wang, M. Cheng, Y. Fan, and K. T. Chau, “A double-stator permanent magnet brushless machine system for electric variable transmission in hybrid electric vehicles,” in *Proc. IEEE Vehicle Power Propuls. Conf. (VPPC)*, Sep. 2010, pp. 1 – 5.

[9]S. Niu, S. L. Ho, and W. N. Fu, “A Novel Double-Stator Double-Rotor Brushless Electrical Continuously Variable Transmission System,” *IEEE Trans. Magn.*, vol. 49, no. 7, pp. 3909–3912, Jul. 2013.

[10]Chuang Yu, KT Chau, JZ Jiang, “A permanent-magnet flux-mnemonic integrated-starter-generator for hybrid electric vehicles,” *IEEE Vehicle Power and Propulsion Conference, 2008, VPPC'08.*

[11]Shuangxia Niu, Yulong Liu, SL Ho, WN Fu, “Development of a Novel Brushless Power Split Transmission System for Wind Power Generation Application,” *IEEE Transactions on Magnetics*, Vol. 50, no. 11, Nov. 2014.

[12]Yunchong Wang, WN Fu, Shuangxia Niu, “A Novel Structure of Dual-Stator Hybrid Excitation Synchronous Motor,” *IEEE Transactions on Applied Superconductivity*, vol. 26, no. 4, Jun. 2016.

[13]Hui Juan Liu, Yue Hao, Shuang Xia Niu, Jing Xiong Zhang, “Performance simulation of flux modulation permanent magnet machines with three topologies,” *Applied Superconductivity and Electromagnetic Devices (ASEMD), 2015 IEEE International Conference on*, Nov. 2015.

[14]Li, F., Chau, K.T., Liu, C., Zhang, Z., “Design principles of permanent magnet dual-memory machines,” *IEEE Trans. Magn.*, 2012, 48, (11), pp. 3234–3237.

[15]Qingsong Wang, Shuangxia Niu, Siu Lau Ho, Weinong Fu, Shuguang Zuo, “Design and analysis of novel magnetic flux-modulated mnemonic machines,” *IET Electric Power Applications*, vol.9, no. 7, pp. 469-477, Jul. 2015.

[16]K. Atallah and D. Howe, “A novel high-performance magnetic gear,” *IEEE Trans. Magn.*, vol. 37, no. 4, pp.129-138, 2001.

[17]Li F. , Chau K.T. , Liu C. , Zhang Z. , “Design principles of permanent magnet dual-memory machines”, *IEEE Trans. Magn.*, 2012, 48, (11), pp. 3234–3237.

[18]C. C. Chan, “The state of the art of electric, hybrid, and fuel cell vehicles,” *Proc. IEEE*, vol. 95, no. 4, pp. 704 – 718, Apr. 2007.

Asian Power Electronics Journal, Vol. 13 , No.1, June 2019

Conceptual Design and Simulation for A Double-Rotor Switched Reluctance Motor Using Parallel Series Windings

Li S. Y[1] Cheng K. W. E[1] Zou Y[1]

Abstract–In this paper, an interchangeable parallel-series winding approach is used to realize a compact machine-housing proposed for the double-rotor motor, based on switched reluctance principle. First, theoretical analyses are elaborated for the concept of the design, combining with the magnetic circuit analysis and given a demonstration by using this approach. Second, the basic mathematical model for the motor is introduced and by using finite element method (FEM), the magnetic field distribution of the motor is acquired and collect torque data, followed by the coupling effects analysis that shows the decoupled magnetic circuits for the two rotors. Finally, to simulate the real working condition, the multi-physical domain simulation is carried out, and high and low speeding operations are obtained. It suggested that the motor is capable of realizing high and low speeds for continuously variable transmission and is expected to be employed by electric vehicles (EVs) and Electric Vessel in the future.

Keywords–Parallel-series-winding, double-rotor motor, switched reluctance, FEM, EVs.

I. INTRODUCTION

Electrical vehicles (EVs) have become a popular candidate for public transportation and many researchers have been investigating and developing, increasingly, under the background of green energy exploring and application. In order to realize a continuously variable transmission (CVT), some traditional EVs adopt intermediate parts such as mechanic and magnetic gears, hydraulic convertors and transferring belts, etc. for speed regulation. To eradicate these intermediate parts and enhance the efficiency for EVs, double-rotor motors have been investigated for EVs. Similar, Electric Vessel also requires the same requirement of transmission. The double-rotor motors have advantages of high traction torque-speed, compact volume and low cost, and most importantly, simultaneous high and low speeds operation [1]. Until now, there are mainly four types of double-rotor motors: direct current (DC) motor, double induction-rotor motor, double switching-flux rotors and double switched-reluctance-rotor motor [2-4]. The difference between the last two motors is that the last one does not own permanent magnets (PMs) [5]. However, all of them are simply designed by integrating two motors into a motor housing, therefore creating two rotors or stators on their corresponding windings. They are usually comprised by two electrical terminals that are roughly equivalent to two motors combining together. For example, ZiXuan's paper [6], has proposed a brushless permanent magnets double-rotors motor for a HEV, and there are two layers of windings with two electric ports for the stator. The same approach for a brushless direct current motor (BLDC) proposed by Durmus Uygun in [3] also simply integrates two DC motors together. In order to avoid the demagnetized influence of permanent magnets, switched reluctance double-rotor motors have been proposed in [7], [8] and this simple approach is employed again. On the other hand, the use of synchronous motor has been applied in vessel but the application to switched-reluctance motor for vessel is not yet reported. It is hard to realize a compact structure if we adopt the simple idea which integrates two identical or different type motors into one machine housing, for these motors are difficult for mass production due to their complex winding slots, and complex flux barriers that should also be taken into account.

Actually, it is essential and necessary by employing or designing simple structures not only for rotors but also for stators and windings as well to effectively realize a compact volume for double-rotor motors of EVs. In this paper, a double-rotor motor based on switched reluctance principle has been proposed. This motor, adopting only one layer of windings fixed on a stator, governs both outer rotor and inner rotor respectively. Put it in another way, both of the two rotors share the same windings to generate torques together. Therefore, the volume of the double-rotor motor can be significantly reduced and simultaneously, low speed and high-speed operations for this motor can be realized readily. Since this motor is a pure switched reluctance motor (SRM) without permanent magnets, it owns all merits that traditional SRMs possess. The paper includes the following contents. First and foremost, the concept of the design has been proposed and then, theoretical analyses are given by using magnetic circuit method so that they verify the effectiveness of the concept. Next, electromagnetic field of the motor are analyzed and calculated by finite element method (FEM), and magnetic coupling analysis is also carried out. Last but not least, a multi-physical field simulation is completed to emulate the real working condition for the motor, which shows the good performance of the motor. It testifies the effectiveness and feasibility of the proposed concept of the motor.

II. THEORETICAL ANALYSIS

1. Magnetic structure of the motor

This motor has two rotors including rotor 1 and rotor 2 shown in Fig.1. Rotor 1 owns a series of teeth that are distributed evenly around within the rotor. Rotor1, stator and rotor2 are comprised by stacked silicon steels. The stator has two poles with small teeth that are identical to that of rotor 1. A pair of coils is wrapped on the two poles for each stator and totally, there are six stators for the motor. Two opposite stators comprise a phase for the motor, which are similar to pure SRM. And all phases are allocated around the rotor 1 with nearly 60 mechanically interval degrees between two adjacent ones. More

---

[1] **Power Electronics Research Centre, Department of Electrical Engineering, The HongKong Polytechnic University, Hong Kong
E-mail: eric-cheng.cheng@polyu.edu.hk**

importantly, as shown in this figure, phase B is aligned with both rotor1 and rotor 2 at the moment. Rotor 2 has two poles and, in the middle part of each pole, there is also a pole with a minimum thickness so that this rotor can realize two step alignments with different lengths of gaps. All rotors and stators are fixed on a shaft by using bearings that are not given in this figure.

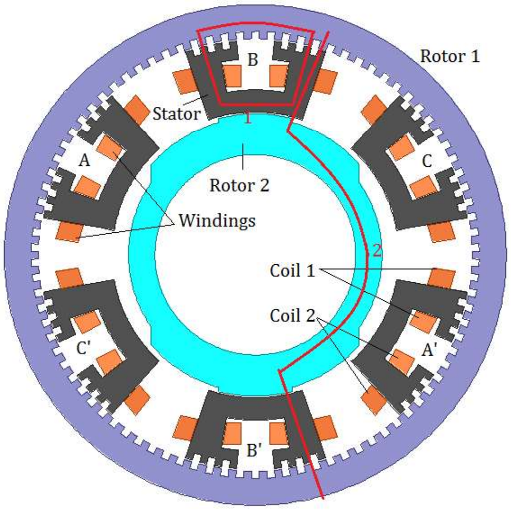

Fig. 1: The structure of the magnetic paths.

2. Theoretical concept

According to the minimum magnetic reluctance principle, the two rotors can be driven by the same stator with current carried windings. Both short flux and long flux paths exist in this motor and when rotor 1 is excited. Under the condition, flux lines would pass through stator to rotor 1 only, crossing the air gaps between them, as shown by the red closed line 1 in Fig.1. When phase AA', CC' and BB' are excited in sequence, the rotor 1 will rotate along anti-clockwise direction. The rotor 2 is driven by the same stators under the long-path flux lines that are shown in Fig.1 highlighted by red line 2. Coincidently, rotor 2 can also rotate in anti-clockwise when phase AA' CC' and BB' are excited in order. The key difference to drive the two rotors is the electric connecting way of the two coils (coil 1 and coil2).

The magnetic paths shown in Fig.1 can be simplified by Fig.2, taking phase BB' as an example. If the two coils of phase B are connected in a serial way and the magnetic circuit for the flux generated by the two coils are shown in the corner of Fig.2. There will be short flux lines passing along the rotor 1 and the stator only. These flux lines cannot influence the status of the rotor 2 because there are no flux lines along the rotor 2. The flux can be expressed as

$$\varphi_1 = \frac{F_1+F_2}{R_1+2(R_S+R_{g1})+R_y} \tag{1}$$

When the two coils of phase B are connected in parallel and then connected with that of phase B' in series, the magnetic circuit for the flux can be shown in Fig.2 and this long flux can be calculated by

$$\varphi_2 = \frac{F_1+F_3}{R_1{'}+R_S+R_{g1}+2R_{g2})+\frac{R_2}{2}} \tag{2}$$

Since the air gaps between the stator and rotor 1 are much smaller than that between the stator and the rotor 2, the flux lines are mainly influenced by the variations of the air gaps *Rg2.* More markedly, there are two different gaps between the stator and the rotor 2, for it has a pair of Y-shaped poles. Therefore, either phase A or phase C excited will drive the rotor to coincide with the central line of the poles, thus driving the rotor 2 rotating in anti-clockwise or clockwise respectively. Torque profiles for rotor 1 and rotor 2 will be discussed in the following part.

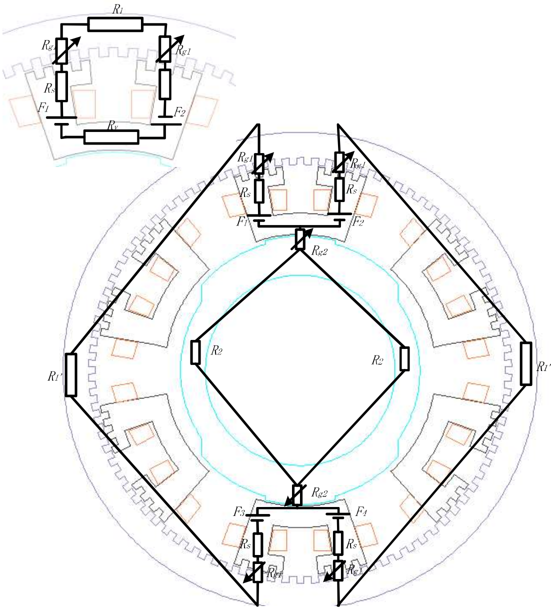

Fig. 2: The equivalent magnetic circuit of the motor.

3. Structure of the electrical driver

How to realize the electrical driver for parallel-series-windings is also a key point for this switched reluctance based drive. Taking one connection of coil 1 and coil 2 as an example, a simple structure for the electrical driver is given in Fig.3.The half bridge topology that is similar to conventional drivers for SRMs is employed, involving two control switches (S1, S2) that are usually high frequent MOSFETs for low power rate motors and two diodes (D1, D2) for freewheeling of the coils (here are coil 1 and coil 2). Particularly, switch 3 (S3), as shown in Fig.3, is used to realize the parallel-series connection for the motor. For there is no need to act for S3 in a super high frequency, a solid-state relay can be employed to realize the driver. As shown in Fig.3 (b), when S3 turns to the upper points and S1, S2 turn on, the current will pass through coil 1 and coil 2 and the two coils are connected in series. After turning off S2 and S3, diodes D1 and D2 will be activated and then the driver enters a freewheeling mode. Similarly, when S3 turns to the lower points, parallel connection for the two coils can be realized as shown in Fig.3 (c). When S1 and S2 turn on, the two coils will be connected in parallel and currents will pass through the two coils separately. After the two switches turn off, the driver will enter into a freewheeling mode and the two coils share two diodes. More importantly, the current directions from the two coils are different. The positive terminal and the negative terminal for the coil 2 should be reversed if we manufacture or connect the coils for the motor. Likewise, this parallel-series connection method can be used for windings as well.

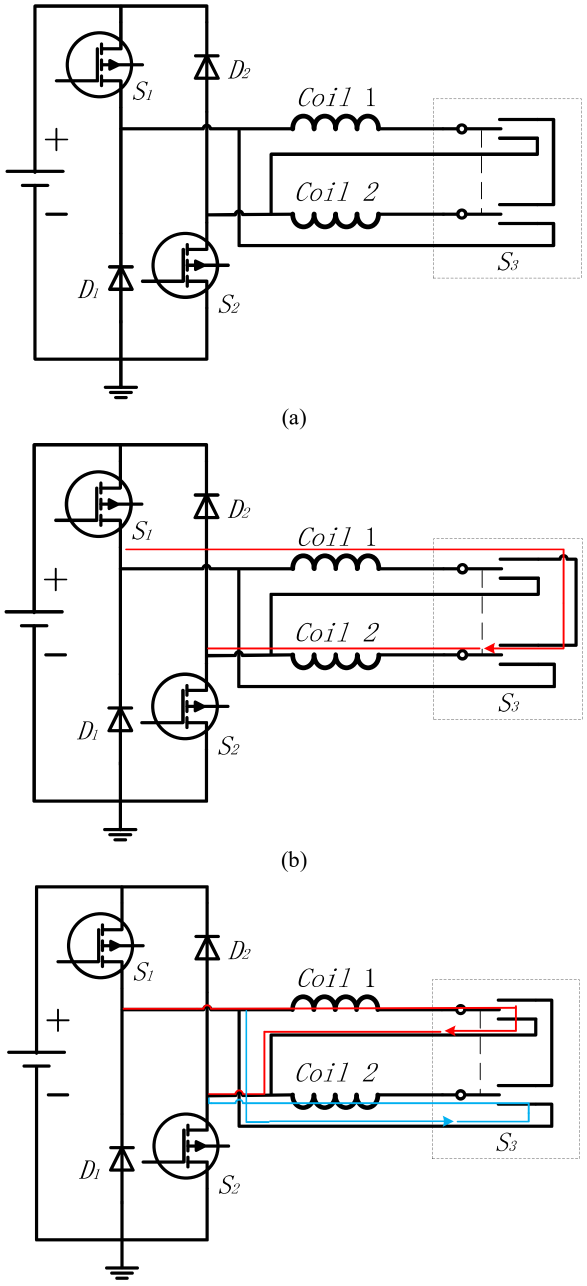

(a)

(b)

(c)

Fig.3: (a) Structure of the driver to realize the parallel-series connection and (b) the two coils connected in series and (c) in parallel.

4. Mathematical model

The motor obeys the principle of maximum reluctance rule that the poles of the rotor 2 and the teeth of the rotor 1 would coincide with that of the stator. The dynamic equation can be expressed as

$$T_j = J_{mj}\frac{d^2\theta_j}{dt^2} + B_j\frac{d\theta_j}{dt} + T_l = \frac{\partial W_j(i,\theta_j)}{\partial \theta_j} \quad j = 1,2 \qquad (3)$$

where, torque T_j is electromagnetic force related to phase currents and angles of the two rotors, J_{mj}, B_j and T_l are load force, mass of mover and damping coefficient respectively. $W_j(i,\theta_j)$ is co-energy of the motor and θ_j is the angles of the two rotors [10], and j represent the number of rotors.

$$W_j(i,\theta_j) = \int_0^i \lambda(i_j,\theta_j)di_j = \int_0^i L(i_j,\theta_j)i_j di_j \qquad (4)$$

$\lambda(i_j,\theta_j)$ is flux linkage of the motor and i_j is the phase current. The value of inductance is a function with phase current and angle of the rotors. According to (3) and (4), we can obtain:

$$T_m = \frac{1}{2}i_j^2\frac{\partial L(i_j,\theta_j)}{\partial \theta_j} \qquad (5)$$

It can be seen that the inductance of the rotor is determined by both the current and angle of the rotor and, the torque output is not linearly related with the current as the nonlinear characteristic of the inductance caused by the phase current and angle of the rotor. The electrical terminal for the motor can be expressed as

$$u_j = R_j i_j + \frac{d\lambda(i_j,\theta_j)}{di_j} \qquad (6)$$

where, R_j, u_j, and i_j represent phase resistance, terminal voltage and current of phase, respectively.

III. FEM ANALYSIS

1. Electromagnetic field

The magnetic field distributions at aligned angle and unaligned angle for the rotor 1 and the rotor 2 are given in Figure 4. It can be seen from Figure 4 (a) and (b) that the flux is concentrated along the stator and the rotor 1 only. Small poles are designed for the rotor 1 to work at low speeds. When the rotor 1 rotates from un-aligned position to aligned position, flux changes obviously in the yoke of the rotor1 and its teeth. By contrast, the flux distributions of other places roughly keep constant. There is little flux crossing the rotor 2. When the windings are connected in parallel way, long flux path dominant the whole area of the motor as shown in Figure 4 (c) and (d). The flux is distributed along the stator, rotor 1 and rotor 2, and the density of the flux is mainly influenced by the angle of the rotor 2. We can see that the flux in both the stator and the rotor 1 and the rotor 2 changes dramatically at different angles of the rotor 2. With the change of the angles of the rotor1 and rotor 2, the inductance changes will play a main role to generate torque. To realize high speed operation by the rotor 2, its pole width is larger than that of the rotor 1 because of high switching frequent. By doing so, the switching frequent can be reduced due to large electric angle between adjacent phases. Hence, the drive of the motor can be achieved easily.

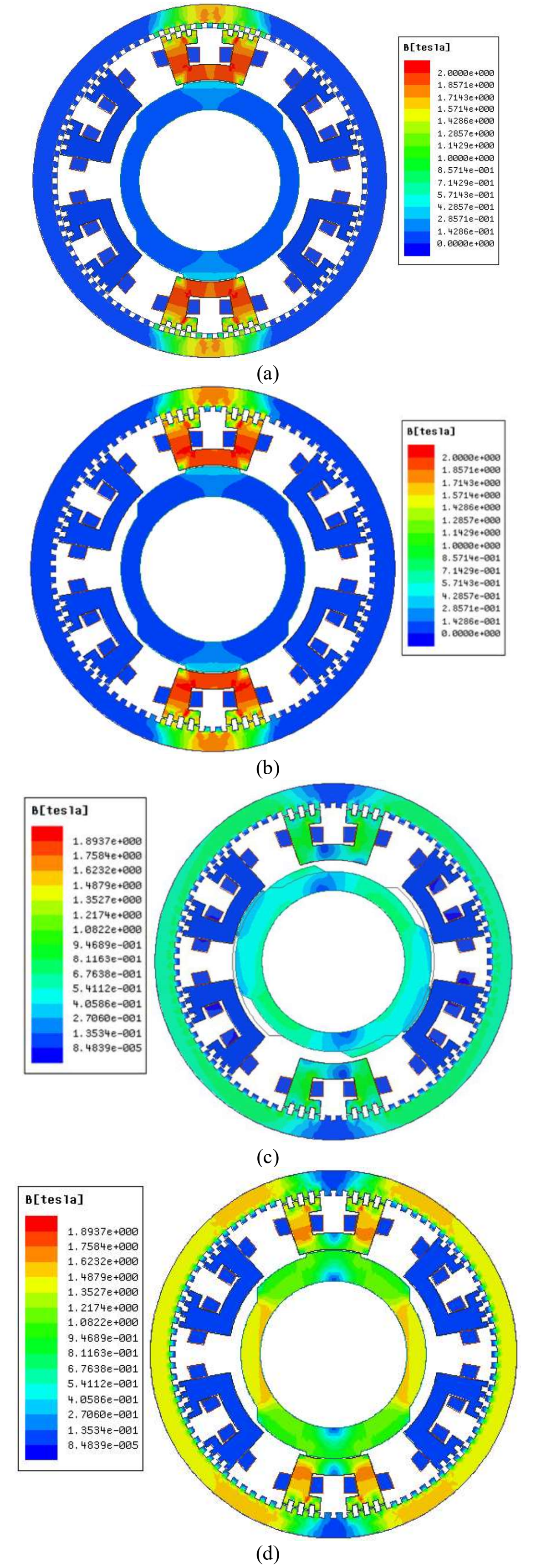

(a)

(b)

(c)

(d)

Fig. 4. Flux density distribution of the motor including (a) short flux path at unaligned angle, (b) short flux path at aligned angle, (c) long flux path at unaligned angle and (d) long flux path at aligned angle.

Inductances and torque outputs with respect to angles are also calculated by FEM as shown in Fig.5. It can be seen from the figure that the values of inductance change dramatically and obviously when the angle of the rotor 1 varies. By contrast, the values experience tiny change when the rotor 2 rotates. Immediately, the latter value is approximately 10 mH less that the former. The average torque output from the rotor 1 is nearly quadrupled than that from the rotor 2. From Fig.5 (d), the torque outputs experience a significant overshoot because of the existence of two lengths of air gaps between the stator and the rotor 2. These torque outputs increase in spite of differing degrees at the beginning with the first air gap increasing from zero to 36 degrees, followed by a sharp drop and then increasing gradually by the degree around 70. Therefore, the second torque outputs are generated from 60 degrees to the end in the whole electrical period of the rotor 2. Rotor 1 can be operated in low speed scope and rotor 2 is suited to realize high speed work.

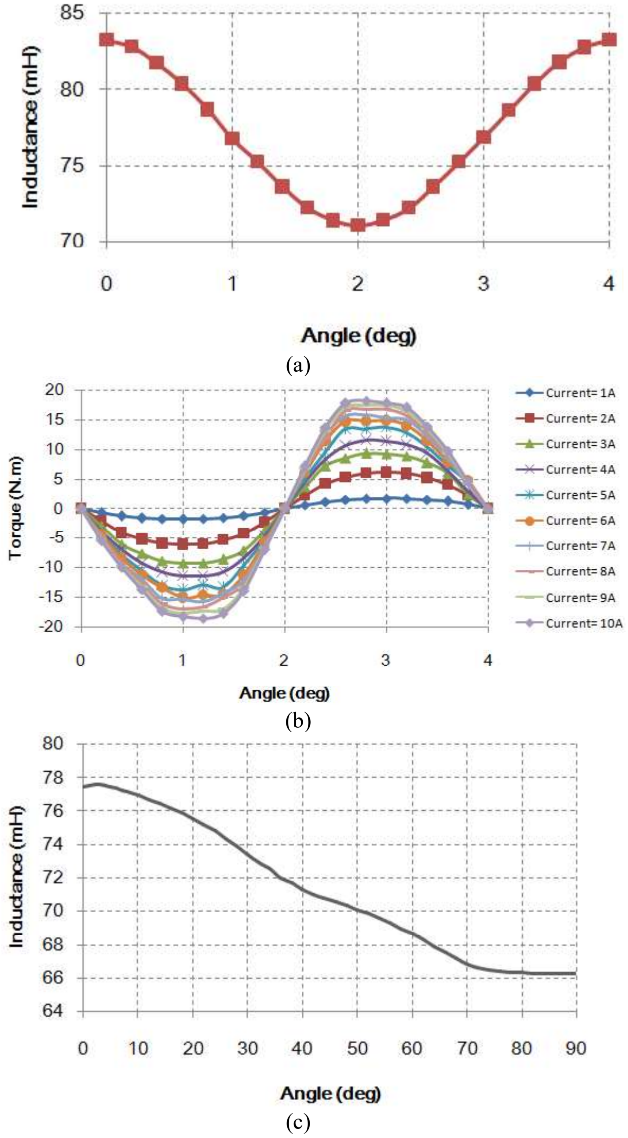

(a)

(b)

(c)

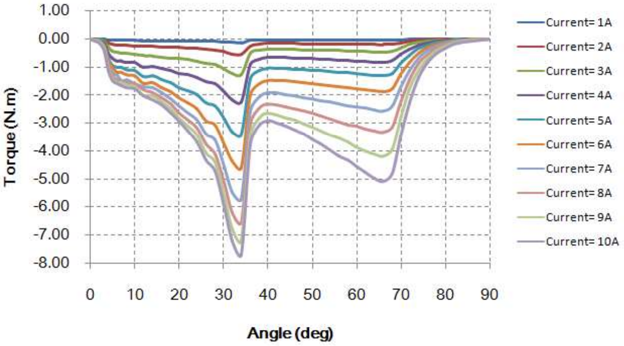

(d)

Fig. 5: Magnetization as a function of applied field.

2. Simulation for parallel-series connection

According to the design of the driver for the motor shown in Fig.3, corresponding simulation modules are built in Fig. 6 (a) to observe the current waveforms when changing the connection status between the two connections. The period of the PWM module is 0.001 s and the period of the pulse is 1 Hz which is used to control the status of the coils connection. It can be seen from Fig. 6 (b), when the series connected coils change to parallel connection, the variations of the two currents of the coils are significant, with the values nearly doubled, experiencing a transient process shown in the circle. The currents can be regulated by the duty of the PWM signal.

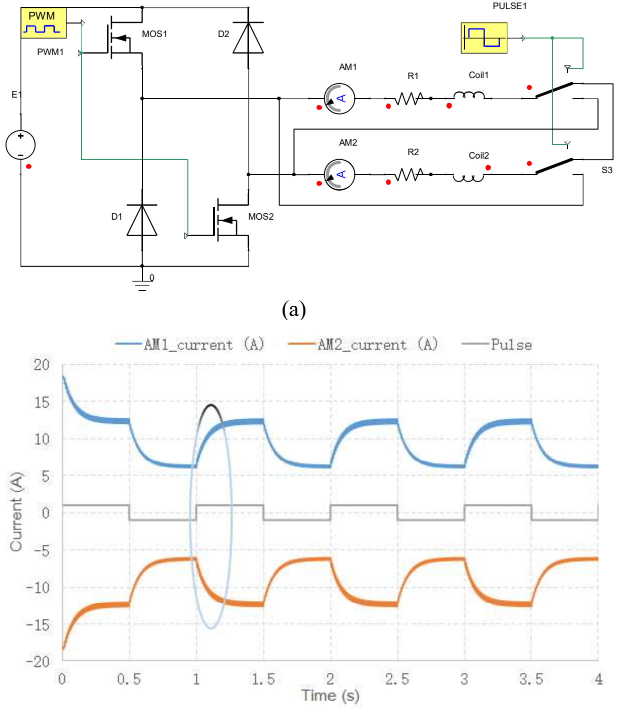

(a)

(b)

Fig.6: (a) Parallel-series connection simulation modules and (b) currents of the two coils.

3. Coupling analysis

From the magnetic field distribution of Figure 4, the short path flux fails to pass the rotor 2. Hence, when the rotor 1 works, the flux generated by the windings of the stator could not influence the rotor 2 and they are nearly magnetically decoupled. Figure 7 (a) shows the torque outputs under the same current level 5 A, when the rotor 1 is at unaligned angle and aligned angle respectively. The torque outputs are approximately equal, which suggests that the angles of the rotor 1 has little impact on the torque output contributed by the rotor 2. Similarly, Figure 7 (b) shows the torque outputs of rotor 1 when the rotor 2 is at unaligned and aligned angles, respectively, with the current excitation 2 A. According the calculation results, there is little coupled influence between the rotor 1 and the rotor 2 so that the magnetic coupled effect can be neglected for the control of the motor.

Table 1: Main Specifications of The Motor

Symbol	Conversion from Gaussian and CGS EMU to SI
Rated power	4.2 W
Rated phase current	10 A
Diameter of the rotor 1	140 mm
Diameter of the rotor 2	60 mm
Number of turns of each coil	200
A average Inductance	75 mH
Stack length	100 mm
Speed range	1-10000 rpm

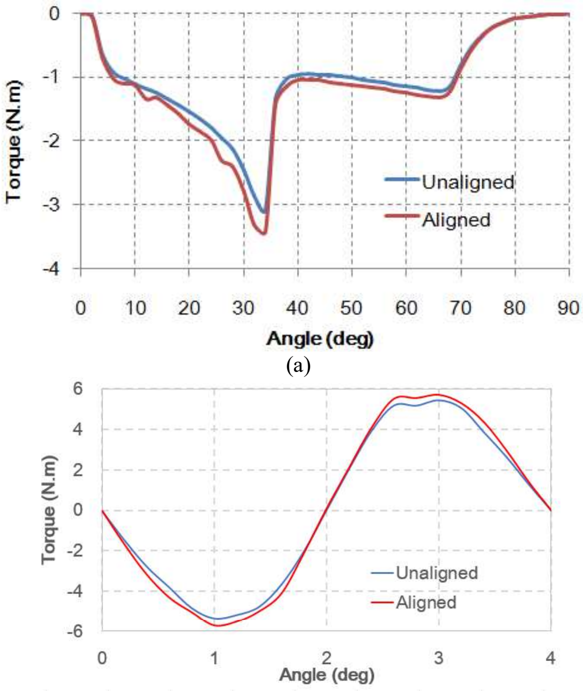

(a)

(b)

Fig. 7: (a) Torque output of rotor 2 from aligned angle to unaligned angle when the rotor 1 is at the unaligned and aligned angles and (b)Torque output of rotor 1 form aligned angle to unaligned angle when the rotor 2 is at the unaligned and aligned angles.

IV. MULTI-PHYSICAL DOMAIN SIMULATION

This section describes the contribution of the paper so that even if readers have not read the body of your paper, they still understand the main idea of the paper. You should not insert any discussion statements in this section because they can be fitted in the previous sections. Even if the author only designed and tested a system, he can also state the achievement in this section. The following statement is an example: The theory has been implemented in an electronic circuit. The circuit has been prototyped and tested. The experimental results agreed very well with the theoretical prediction and verified the theory proposed.

In order to simulate the real working condition for the motor, the multi-physical domain simulation platform is built and it mainly includes four parts that are electrical part, mechanical part, FEM module and control part, as shown in Fig.8. The electrical part consists of a power supplier, a capacitor and a three-phase asymmetric half bridge topology, comprising the drive for the motor. The mechanical part involves damping and mass elements to set the physical parameters for the motor. The control part is built by using C language module to calculate the current for each phase, according to the feedbacks of angle and angular speed, thus obtaining the turn-on and turn-off angles for the motor in the end. The FEM module is established by using finite element analysis and the basic specifications of the motor are listed in the Table I.

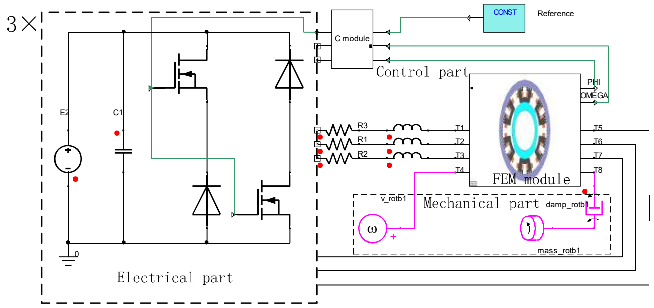

Fig. 8: Multi physical simulation platform for the motor

The speed control block can be simply expressed by Fig.9. It mainly includes three parts that are the controller, the driver and the motor. The controller outputs current reference to the driver after regulating the error of reference angular speed and the real angular speed of the motor. Importantly, for the current regulation part, we select different current regulation methods for high speed and low speed operations of the motor. In high speed, two specific angles are chosen to turn on and turn off the switches during an entire electrical period for each phase. By contrast, the current pulse width modulation (PWM) is employed to regulate the phase currents.

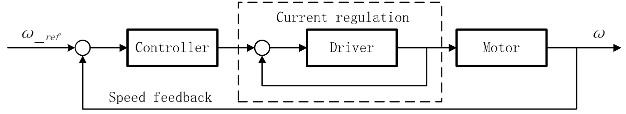

Fig. 9; The speed control block of the motor.

When the motor works in high speed, the torque outputs and speeds are given in Fig.10. From the simulation results, it can be seen that its torque output will decrease with the rise of the speed. From Fig.10 (b), with the speed increases, the load toque experiences high loading torques that exceed 15 Nm, followed by a sharp decline and reach a steady load at average 1 Nm. The speed experiences an acceleration and increases from zero to 10000 rpm, entering a steady status by the end. The results verify that the motor is capable of operation in high speed.

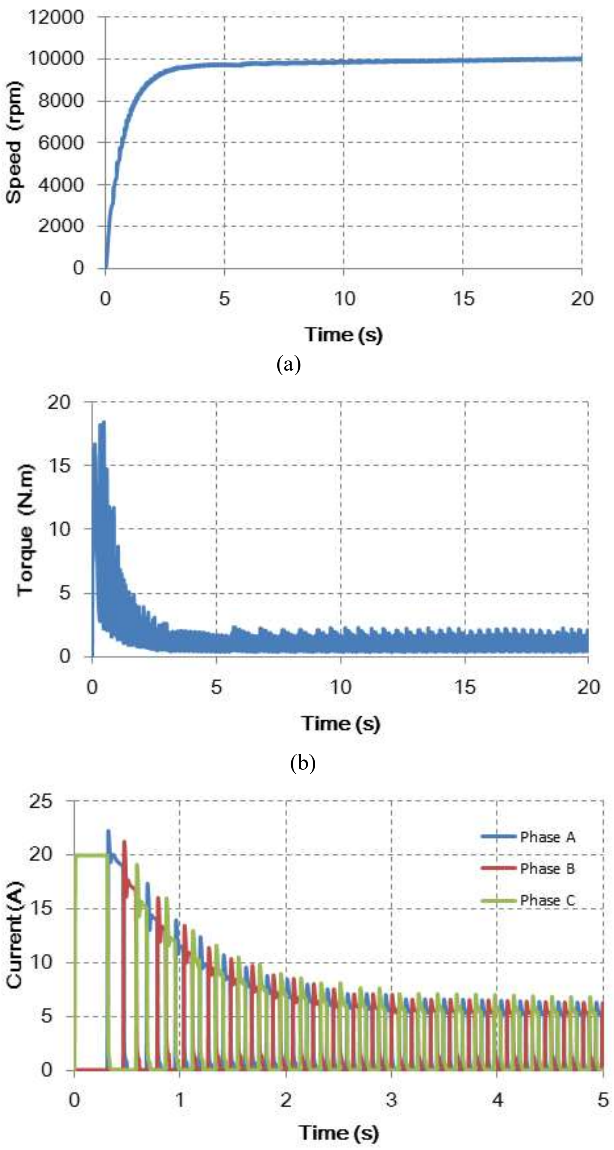

(a)

(b)

(c)

Fig. 10: (a) the speed curve of the motor with average torque load (b) and currents of three phases (c).

When the motor operates in low speed, the phase currents should be controlled by the method of pulse width modulation (PWM) to curb their maximum values. As shown in Fig.11 (a), the speed waveform and three phase currents indicate the capability of the motor starting with load of 2.5 Nm. By PWM control, currents are regulated at around 6 A, and we can see the accelerating process of the motor, with speed gradually increases from zero to approximate 13.5 rpm within 5 minutes. Fig.11 (b) shows the torque output of the motor under a low speed condition. It can be seen that there is some torque ripple under a low speed working condition for this motor. Although there is some torque ripple in low speed, advanced control algorithms could be developed to mitigate or avoid the ripple. In short, the motor can work in both high speed with angle-position control and low speed with current PWM control.

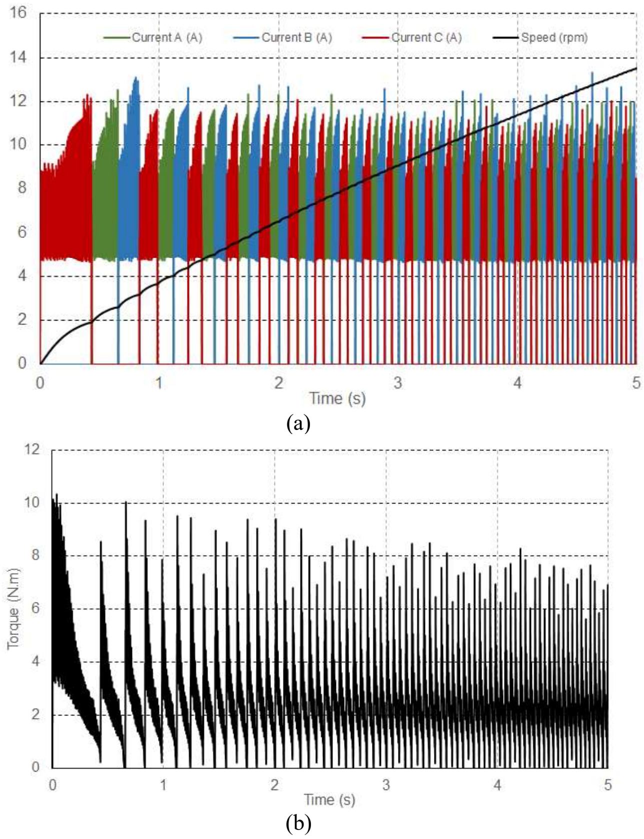

(a)

(b)

Fig. 11; (a) the speed and three phase currents with PWM control under load and (b) corresponding torque output.

V. CONCLUSION

Connecting windings by interchanging parallel and serial circuits is an effective way to integrate double-rotor motors based on switched reluctance principle. Both the theoretical analysis and simulations suggest that by using this approach, the integrated motor with a compact structure is able to realize high and low speeding operations simultaneously, thus achieving a variable transmission for EVs. Meanwhile, finite element analyses confirm that the coupling effect for the motor can be ignored. A forthcoming study on this motor will be carried out, including information on parameter optimizations and manufacturing and controller designs for the motor, etc. The proposed design concept lays a new path for the double-rotor switched reluctance motor that is expected to be employed in EVs, HEVs and Electric Vessels in the future due to its performance in speed and torque.

ACKNOWLEDGMENT

The authors gratefully acknowledge the support from The Research Committee, The Hong Kong Polytechnic University under project reference G-YN27.

REFERENCES

[1] Joachim Druant, Frederik De Belie, Peter Sergeant and Jan Melkebeek, "Concept Study of a Double Rotor Induction Machine used as Continuously Variable Transmission," IEEE international Electric Machines & Drives Conference (IEMDC), pp.656-661,2015.

[2] Johannes H. J. Potgieter Maarten J. Kamper, "Double PM-Rotor, Toothed, Toroidal-Winding Wind Generator: A Comparison with Conventional Winding Direct-Drive PM Wind Generators Over a Wide Power Range", IEEE Transactions on Industry Applications, vol. 52, no. 4, JULY/AUGUST pp.2881-2890, 2016.

[3] Durmus Uygun, Selim Solmaz, Yucel Cetinceviz, "Dual Stator/Rotor Brushless DC Motors: A Review of Comprehensive Modelling Based on Parametric Approach and Coupled Circuit Model," 2015 Intl Aegean Conference on Electrical Machines & Power Electronics (ACEMP), pp.635-641, sep, 2015.

[4] Zixuan Xiang, Li Quan, Xiaoyong Zhu, and Lin Wang, "A Brushless Double Mechanical Port Permanent Magnet Motor for Plug-In HEVs," IEEE Transactions on Magnetics, vol. 51, no. 11, pp.8111104, 2015.

[5] Yinye Yang, Nigel Schofield, Ali Emadi, "Double-rotor switched reluctance machine design, simulations, and validations," IET Electrical Systems in Transportation, vol.6, no. 2, pp.117-125, 2016.

[6] Zixuan Xiang, Xiaoyong Zhu, Li Quan, Yi Du, Chao Zhang, Deyang Fan, "Multilevel Design Optimization and Operation of a Brushless Double Mechanical Ports Flux-Switching Permanent Magnet Motor", IEEE Transactions on Industrial Electronics, 2016 (early access)

[7] Yinye Yang, Nigel Schofield, and Ali Emadi, "Double-Rotor Switched Reluctance Machine (DRSRM)," IEEE Transactions on Energy Conversion, vol. 30, no. 2, pp.671-680, JUNE 2015.

[8] Chuang Yu, Shuangxia Niu, S. L. Ho, and W. N. Fu, "Magnetic Circuit Analysis for a Magnetless Double-Rotor Flux Switching Motor," IEEE Transactions on Magnetics, col. 51, no. 11, pp.8111905, NOVEMBER 2015.

[9] Anbin Chen; Xiaokun Liu; Fengyu Xu; Jiwei Cao; Liyi Li, "Design of the Cryogenic System for a 400 kW Experimental HTS Synchronous Motor", IEEE Transactions on Applied Superconductivity, 2010, Vol. 20, Issue 3, pp. 2062 – 2065.

[10] T. J. Miller, Electronic control of switched reluctance machines, Newnes Power Engineering Series: U.S., pp.68-72, 2001.

BIOGRAPHY

Li Siyang obtained his BSc degrees from the South China University of Technology in 2012. He is currently pursuing his Ph.D degree under the supervision of Professor Cheng at the Power Electronics Research Centre in the Hong Kong Polytechnic University.

Her research interest mainly focuses on the, Energy conversion, Solar tracking system for CPV power generation system, Design and control the SR motor, as well as energy storage,

K.W.E.Cheng obtained his BSc and PhD degrees both from the University of Bath in 1987 and 1990 respectively. Before he joined the Hong Kong Polytechnic University in 1997, he was with Lucas Aerospace, United Kingdom as a Principal Engineer.

He received the IEE Sebastian Z De Ferranti Premium Award (1995), outstanding consultancy award (2000), Faculty Merit award for best teaching (2003) from the University and Silver award of the 16th National Exhibition of Inventions. He has published over 200 papers and 7 books. He is now the professor and director of Power Electronics Research Centre.

Yu Zou obtained his B.S. degree from Hubei University in 2010 and Master degree at College of Mechatronics and Control Engineering at Shenzhen University in 2013. He is now pursuing his Ph.D degree at The Hong Kong Polytechnic University.

Asian Power Electronics Journal, Vol. 13 , No.1, June 2019

Investigation on Advanced Control of A Linear Switched Reluctance Motor

Zou Y Cheng K. W. E Cheung N. C

Abstract–Advanced control systems are increasingly employed for intelligent factories. Fuzzy logic control (FLC) and backward propagation neural network (BPNN) control are investigated in this paper to realize position control for a linear switched reluctance motor (LSRM) against its nonlinear characteristics. Principles for FLC and BPNN control are introduced elaborately. Simulation results via BPNN show that dynamic position errors for the LSRM can be limited to 0.1 mm. Experimental results on FLC suggest that point-to-point position tracking for the motor can achieve 0.01 mm, constraining dynamic position error in 0.1 mm. By experiments, FLC for the LSRM performs better than traditional proportional-integral-derivative (PID) control, proving the effectiveness of the alleviation of the nonlinearity for the LSRM.

Keywords–Fuzzy logic control, backward propagation neural network, LSRM, position tracking.

I. INTRODUCTION

Intelligent control algorithms are introduced to improve the performance of linear motors for precisely positioning trackers with high stability, because of uncertainties on the motors caused by their nonlinear characteristics and interferences from circumstance [1]. A liner switched reluctance motor (LSRM) as one of the linear motors is the control plant in this paper. The nonlinearity of the motor exists due to saturated magnetic cores, nonlinear thrust outputs and variety between static fraction coefficients and moving fraction coefficients [2]. Meanwhile, interference caused by varied loads, coupled flux lines and drifted parameters may significantly deteriorate the performance of the motor. Employing traditional PID controller is unable to fulfill the requirements of good performance under these uncertainties. Therefore, advance control approaches are increasingly investigated to address those problems mentioned. To solve the deteriorated performance stemmed from nonlinearity and altered operation conditions of the motor, fuzzy logic control (FLC), neural network control (NNC), adaptive control and sliding mode control (SMC) are used to control the position of the motor [3-6]. These control methods can imitate expert's experience, compute and exert adjusted control commands for the motor to get a satisfactory performance. After using these advanced controllers, not only will the overall hardware cost on the motion system reduce, but also the motor performance becomes better. Among them, FLC can transform linguistic control rules from experts' knowledge to regulate behaviors of mechanical devices, regardless of their accurate mathematic models [3]. Consequently, the controller would become simple and easy to design and implement. For industry control, most processes are suited to use linguistic rules, especially for those complex systems that their dynamic models are difficult to obtain or precisely predict. After imitating what the experts' programed, the controller would become intelligent. BP NNC is a popular intelligent control method. This method is capable of addressing nonlinear issues for the whole system because of its multiple layer mapping transformations with nonlinear characteristics [4]. Also, self-teaching and self-adaptation can optimize the weights of nodes, thus improving the performance of the motor and enhancing the stability of the system [5]. Except for these merits, BP NNC has high fault-tolerant capability so that the whole system would become more robust. Adaptive control is an effective approach to avoid the influences of altered environment or parameters. The designed zeros or poles for the motor will be regulated after identifying the parameters of the controlled subject. For the motor, in this paper, the position of the motor can be controlled and regulated after identifying the dynamic parameters of the operated motor [5]. Accordingly, the controlled position will be modified with more accuracy even though the parameters of the motor vary with the time. Sliding mode control (SMC) is another advanced control to address the nonlinear behavior of the control plant [6]. The core to design the SMC is to find a suitable sliding mode surface for the motion system.

In this paper, fuzzy logic control and BP neural network control approached mentioned are designed for the motor. Simulation and experimental results are obtained. After comparing the controlled results, advantages from each advanced controller are yielded, with elaborated analysis for the obtained results.

II. INTRODUCTION FOR THE LSRM

A. Configuration of LSRM

The basic mechanical structure of the LSRM is shown in Fig.1. This motor consists of three phase windings and each winding possesses a coil wrapped around a steel stacked core. Three cores fixed on an aluminum plate constitute the mover of the motor. Their section views are shown in Fig.1. The mover connected with four slippery wheels that belong to the components of two linear guides. The linear guides as well as the stator that is also comprised of stacked steel plates are fixed on a basement, which is the stator base. A 1-μm-resolution linear optical encoder is integrated into the LSRM system to observe the motion profile of the moving platform and provide the feedback position information. The main electrical and mechanical parameters of the LSRM are listed in Table I.

**Power Electronics Research Center, Department of Electrical Engineering,
The Hong Kong Polytechnic University, Hong Kong.
Email: yy.zou@connect.polyu.hk eeecheng@polyu.edu.hk norbert.cheung@polyu.edu.hk**

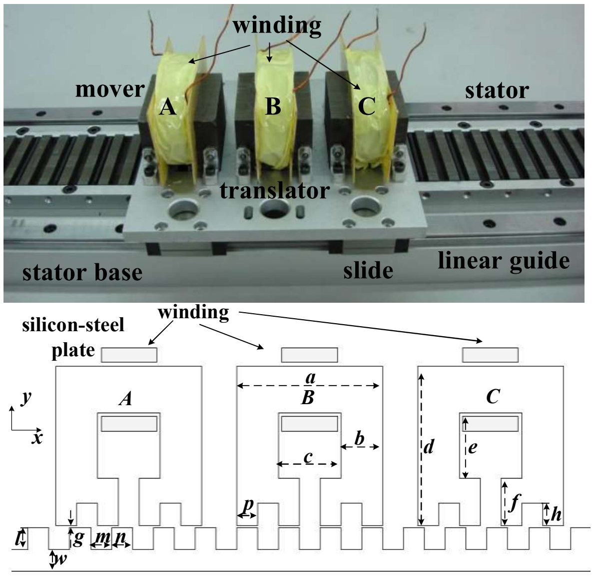

Fig. 1: The sections views of the motor.

Table 1: Specifications of the LSRM

Parameters	value
Rated current	4A
Mass of moving platform	1.5kg
Mass of stator	2kg
Pole width	6mm
Pole pitch	12mm
Phase division	10mm
Phase resistance	2ohm
Air gap length	0.3mm
Number of turns	160
Stack length	25mm
Encoder resolution	1µm
Rated current	4A
Mass of moving platform	1.5kg

B. Dynamic model of LSRM

The electrical terminal for any one phase can be characterized as the voltage balancing equation as follows:

$$u = R\cdot i + \frac{d\lambda(i,x)}{dt} \quad (1)$$

where R, u and i represent phase resistance, terminal voltage and current, respectively. x is displacement and $\lambda(i,x)$ denotes flux-linkage. From the mechanical side

$$F = M\frac{d^2x}{dt^2} + B\frac{dx}{dt} + f_L = \frac{1}{2}\cdot i^2 \cdot \frac{fL(i,x)}{fx} \quad (2)$$

where F is electromagnetic force, f_L, M and B are load force, mass of moving platform and friction coefficient, respectively.

C. Nonlinearity of the LSRM

As the saturation phenomenon of the magnetic steel materials exists and nonlinearity for the motor will occur. All motors cannot avoid the nonlinearity. The LSRM, as one of the motors, has a highly nonlinear characteristic. According to equation (2), if the input command is a force reference, this force command can be transformed as a current reference for drivers of the motor. Also, to improve the performance of the motor, force distribution function (FDF) is an effective way to alleviate the nonlinear force outputs excited by phase currents [5]. The overall FDF scheme is shown in Fig.2. Force ripples and acoustic noise generated by the motor can also be mitigated via a reasonable FDF that is designed to match the electromagnetic behavior of the motor. Apart from this approach, the advanced control method introduced as the following can also address the nonlinear problem. However, advanced control algorithms are usually employed for the motor to get a better performance against the nonlinearity.

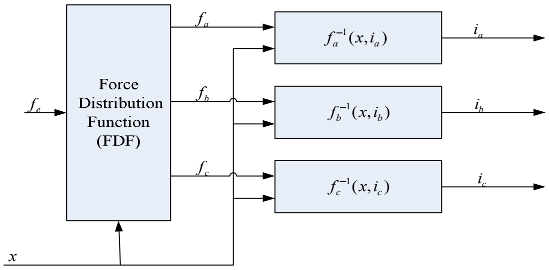

Fig. 2: The structure of the FDF.

III. ADVANCED CONTROL FOR THE LSRM

A. Configuration of control

This motor is suitable for a fuzzy PD controller. This controller can adjust control parameters according to the status of the motor via fuzzy logic approach. The fuzzy logic mainly consists of fuzzification, rule bases, fuzzy reasoning and defuzzifier. K_p and K_d are the proportional gain and the differential gain of the PD controller, respectively. The control diagram is shown in Fig. 3.

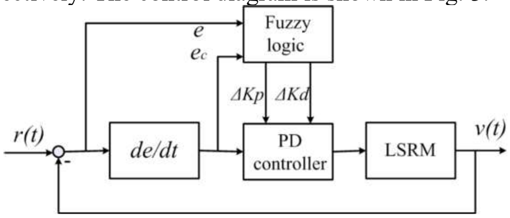

Fig. 3: FLC diagram for the LSRM.

The proposed fuzzy PD controller takes the position error and its change as the inputs and outputs the values of K_p and K_d. The two coefficients can be formulated as

$$K_d = K_{d0} + \Delta K_d \quad (3)$$

$$K_p = K_{p0} + \Delta K_p \quad (4)$$

where K_{p0} and K_{d0} are the initial values ,ΔK_p and ΔK_d are the increases of K_p and K_d.

By using the feedback signal from a position sensor, position error *E* and its change rate *Ec* can be obtained. The fuzzy logic controller will employ the two values. In this paper, the regions of the fuzzy sets for the two parameters are {-6 -4 -2 0 2 4 6}. After fuzzification, the fuzzy set values will be {NB NM NS ZO PS PM PB} and the corresponding linguistic variable fuzzy set is [negative large, negative middle, negative small zero, positive small, positive middle, positive big], as shown in Fig.4. Similarly, the discussion region for K_d and K_p are given in Fig.5. The rule bases for K_p and K_d are listed in Table II and III.

In this paper, we choose the triangle membership function for *E*, *Ec*, K_p and K_d, Mamdani inference method for fuzzy reasoning, and the center of gravity method for defuzzification.

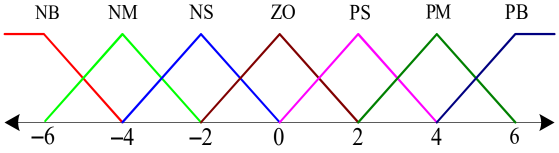

Fig.4: Membership functions of *E* and *Ec*.

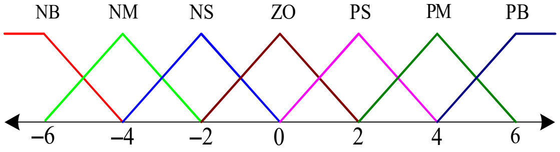

Fig.5: Membership functions of K_p and K_d.

The basic control rule for the fuzzy logic controller mainly includes:

(1) When |*E*| is large, to achieve a stronger dynamic response performance, we can set larger K_p and smaller K_d.

(2) When |*E*| is medium size, in order to obtain a smaller overshoot of the system response, K_p can be set smaller. At this time, K_d can be set larger.

(3) When |*E*| is small, to make the system stable, the value of K_p should be set smaller. To avoid the system oscillation near the set value, the value of K_d should refer to the value of |*Ec*|. When the value of |*Ec*| is small, the value of K_d can be larger. In contrast, when the value of |*Ec*| is larger, the value of K_d can be small.

Table II: Rule base of the K_p

E \ EC	NB	NM	NS	ZO	PS	PM	PB
NB	PB	PB	PM	PM	PS	ZO	ZO
NM	PB	PB	PM	PS	PS	ZO	NS
NS	PM	PM	PM	PS	ZO	NS	NS
ZO	PM	PM	PS	ZO	NS	NM	NM
PS	PS	PS	ZO	NS	NS	NM	NM
PM	PS	ZO	NS	NM	NM	NM	NB
PB	ZO	ZO	NM	NM	NM	NB	NB

Table III: Rule base of the K_d

E \ EC	NB	NM	NS	ZO	PS	PM	PB
NB	PS	NS	NB	NB	NB	NM	PS
NM	PS	NS	NB	NM	NM	NS	ZO
NS	ZO	NS	NM	NM	NS	NS	ZO
ZO	ZO	NS	NS	NS	NS	NS	ZO
PS	ZO	ZO	ZO	ZO	ZO	ZO	ZO
PM	PB	NS	PS	PS	PS	PS	PB
PB	PB	PM	PM	PM	PS	PS	PB

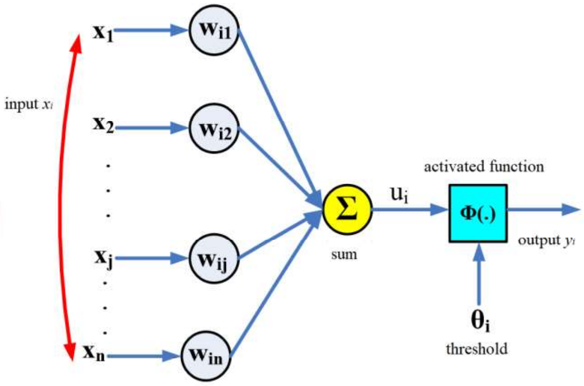

Fig.6: Model of an artificial neuron.

B. Artificial neural network

Neuron here is the basic processing unit for the artificial neural network. Generally, it consists of multi inputs and a single output, processing nonlinear signals. A neuron includes a connector with a weight value, a sum unit and an activated function. A neuron with a series of inputs x_1, $x_2, \ldots, x_n$ of connectors with weights $w_1, w_2, \ldots, w_n$ is shown in Fig.6. y_i is the output of the neuron i. After summing, a linear integrity output u_i is yielded through these y_i. $y_i = \varphi(\cdot)$ is the activated function with a threshold θ_i to constrain the output scope of the designed neuron. The mathematical model for the neuron can be expressed as

$$u_i = \sum_{j=1}^{n} w_{ij} x_j \quad , \tag{5}$$

$$net_i = u_i - \theta_i \quad , \tag{6}$$

$$y_i = \varphi(net_i) \, . \tag{7}$$

where net_i denotes a computing method to combine these inputs.

a) Backward Propagation neural network

Back propagation (BP) neural network is one kind of neural network and it can be also named as a backward propagation network or a multi-level forward network.

BP algorithm is an optimal method based on gradient downward approach, adjusting the weight to minimize the overall error of the network. It comprises forward network computation and error inverse propagation. These weights for neurons will be optimized after backward transferring errors to minimize the overall error of the controlled system. BP network usually involves an input layer, a hiding layer and an output layer. A BP network is shown in Fig. 7, with the numbers of the inputs, the outputs and the implicit node *m*, *n* and *q*, respectively.

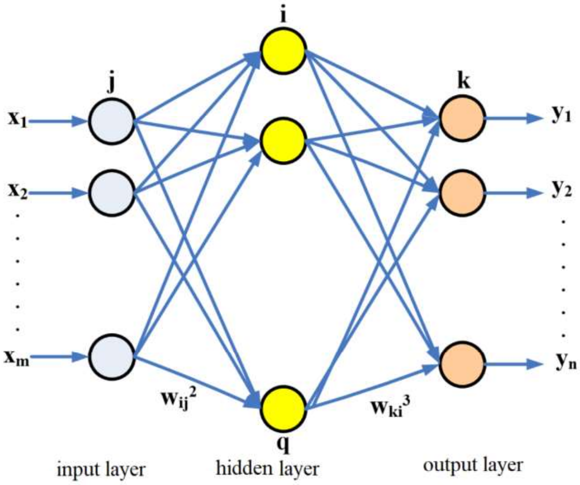

Fig.7: The structure of the BP neural network.

b) BP forward network design

The outputs of the input layer of the BP network can be expressed as

$$O_j^1 = x_j, (j = 1, 2, ..., m) \tag{8}$$

The inputs and outputs of the implicit layer are

$$net_i^{\ 2} = \sum_{j=1}^{n} w_{ij}^{\ 2} O_j^1 - \theta_i, (i = 1, 2, ..., q) \tag{9}$$

$$O_j^2 = \varphi(net_i^{\ 2}) \tag{10}$$

Inputs and outputs of the output layer can be formulated as

$$net_k^{\ 3} = \sum_{i=1}^{q} w_{ki}^{\ 3} O_i^1 - \theta_k, (k = 1, 2, ..., n) \tag{11}$$

$$O_j^3 = \varphi(net_i^{\ 3}) \tag{12}$$

where O_j^1, O_i^2, O_k^3 are outputs of the input layer，and $net_i^{\ 2}$, $net_i^{\ 3}$ are inputs of the complicit layer and the output layer. $w_{ij}^{\ 2}$ and $w_{ij}^{\ 3}$ are connecting weights between the input layer, the implicit layer and the output layer. θ_i, θ_k are thresholds of the implicit layer and the output layer. $y_i = \varphi(\square)$ is the activated function expressed by

$$\varphi(x) = \frac{1}{1 + e^{-x}} \tag{13}$$

$$\varphi(x) = \frac{1 - e^{-x}}{1 + e^{-x}} \tag{14}$$

c) Regulation of PB neural network via error

The output error of the system is

$$J = \frac{1}{2} \sum_{k=1}^{n} (r_k - y_k)^2 \tag{15}$$

where r is the reference of the system and y is the output.

d) Weight regulation of output layer

Weights, as weighting factors of the output layer, will adjust according to the negative value of the gradient to function *J*

$$\Delta w_{ki}^3 = -\eta \frac{\partial J}{\partial w_{ki}^3} = -\eta \frac{\partial J}{\partial net_{ki}^3} \cdot \frac{\partial net_{ki}^3}{\partial w_{ki}^3} \tag{16}$$

where η is a learning rate, $\eta > 0$.

And

$$\frac{\partial net_{ki}^3}{\partial w_{ki}^3} = O_i^2 \tag{17}$$

$$\frac{\partial J}{\partial net_k^3} = \frac{\partial J}{\partial O_k^3} \cdot \frac{\partial O_k^3}{\partial net_k^3} = -(r_k - y_k) \cdot \varphi'(net_i^{\ 3}) \tag{18}$$

assuming that

$$\delta_k = (r_k - y_k) \cdot \varphi'(net_i^{\ 3}) \tag{19}$$

Then

$$\Delta w_{ki}^3 = \eta (r_k - y_k) \cdot \varphi'(net_i^{\ 3}) \cdot O_i^2 = \eta \delta_k O_i^2 \tag{20}$$

it can be rewritten as

$$w_{ki}^3(k+1) = w_{ki}^3(k) + \Delta w_{ki}^3 = w_{ki}^3(k) + \eta \delta_k O_i^2 \tag{21}$$

to improve the convergent rate of the computing results, the weights can be modified as

$$\begin{aligned} w_{ki}^3(k+1) &= w_{ki}^3(k) + \eta \delta_k O_i^2 \\ &+ \alpha (w_{ki}^3(k) - w_{ki}^3(k-1)) \end{aligned} \tag{22}$$

where α is an inertia coefficient and $0 < \alpha < 1$.

e) Weight regulation of implicit layer

According to the gradient of *J*, the weights for the implicit layer can be calculated as

$$\Delta w_{ki}^2 = -\eta \frac{\partial J}{\partial w_{ki}^2} = -\eta \frac{\partial J}{\partial net_{ki}^2} \cdot \frac{\partial net_{ki}^2}{\partial w_{ki}^2} \tag{23}$$

where η is a learning rate, $\eta > 0$.

And

$$\frac{\partial net_{ki}^2}{\partial w_{ki}^2} = O_i^1 \tag{24}$$

$$\frac{\partial J}{\partial net_k^2}=\frac{\partial J}{\partial O_k^2}\cdot\frac{\partial O_k^2}{\partial net_k^2}=-(r_k-y_k)\cdot\varphi^{'}(net_i^{2}) \qquad (25)$$

the output of the implicit layer will put an impact on all units connected with the unit from the layer

$$\begin{aligned}\frac{\partial J}{\partial O_k^2}&=\sum_{k=1}^{n}\frac{\partial J}{\partial net_k^3}\cdot\frac{\partial net_k^3}{\partial O_k^2}\\&=\sum_{k=1}^{n}\frac{\partial J}{\partial net_k^3}\cdot w_{ki}^3=-\sum_{k=1}^{n}\delta_k\end{aligned} \qquad (26)$$

given that

$$\delta_i=-\sum_{k=1}^{n}(\delta_k\cdot w_{ki}^3)\cdot\varphi^{'}(net_i^{3}) \qquad (27)$$

then

$$\Delta w_{ki}^2=\eta\sum_{k=1}^{n}(\delta_k\cdot w_{ki}^3)\cdot\varphi^{'}(net_i^{2})\cdot O_i^1=\eta\delta_k O_i^1 \qquad (28)$$

it can be rewritten as

$$w_{ki}^2(k+1)=w_{ki}^2(k)+\Delta w_{ki}^2=w_{ki}^2(k)+\eta\delta_k O_i^1 \qquad (29)$$

likewise, to improve the convergent rate of the computing results, the weights can be modified as

$$\begin{aligned}w_{ki}^2(k+1)&=w_{ki}^2(k)+\eta\delta_k O_i^1\\&+\alpha(w_{ki}^2(k)-w_{ki}^2(k-1))\end{aligned} \qquad (30)$$

where α an inertia coefficient and $0<\alpha<1$.

f) BP neural network PID control

BP network is capable of self-learning and nonlinear adaption. BP network PID control is to seek the optimal control parameters for the PID controller by self-learning of the BP network. The whole control block can be plotted as in Fig. 3. *r* is the reference and y is the output. *e* is the error of the system. u is the output of the system controller. *Kp*, *Ki* and *Kd* are the control parameters for the PID controller, obtained from the BP network. These parameters for the PID controller and the BP network are the two key parts for the whole control of the system. According to the status of the system, BP network can enter a self-learning to adjust the parameters for the PID controller so that the adaptive and nonlinear control will be realized.

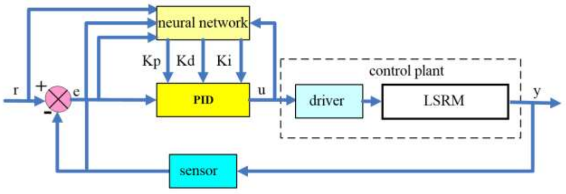

Fig.8: PID control scheme with neural network for the LSRM.

IV. VERIFICATION OF THE ADVANCED CONTROL

To verify the effectiveness of the mentioned advanced control algorithms, simulation software MATLAB/Simulink is introduced to build the controllers including fuzzy logic control and BP neural network control. After building the simulation block via Simulink, simulation results are obtained for neural network PID controller, as shown in Fig. 9. Fig. 9 (a), (b) and (c) show the values of the coefficients K_p, K_i and K_d, respectively. Fig.9 (d) and (e) illuminate the position tracking and its errors. Position tracking errors corresponding to a sinusoidal reference can be limited less than 0.1 mm under the steady status of the motor. Meanwhile, by programing the Simulink control blocks of fuzzy logic control into dSPACE card, a hardware controller for the fuzzy logic control of the linear motor is established. Experimental results are shown in Fig. 10. Position tracking errors are constrained in 0.1 mm for sinusoidal reference and 0.01 mm for square wave reference, respectively. Both sinusoidal and square wave references validate the effectiveness of the designed fuzzy logic controller.

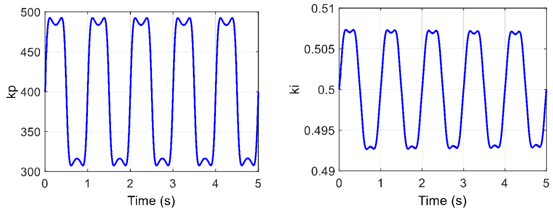

(a) Values of K_p for BPNN (b) Values of K_i for BPNN

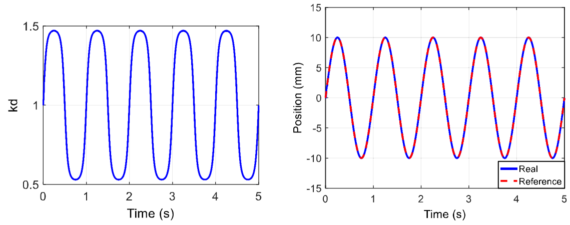

(c) Values of K_d for BPNN (d) Position response controller

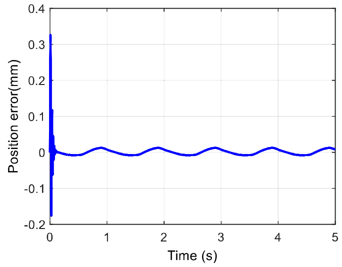

(e) position error of the BPNNC control system

Fig. 9: Coefficients (a), (b), (c) and (d) position response and errors (e) for the designed BPNN control.

The comparison of PID controller and fuzzy logic PID controller are shown in Fig.10. From the experimental results especially under a sinusoidal reference, position errors from the fuzzy logic controller are less than that from a PID controller, which obviously shows that advanced control can improve the performance of the LSRM, particular under a varied reference. Although the performance of the LSRM under the reference could be worse as different operation status with nonlinear factors, advanced control motion system outweigh traditional equipment and can perform better in industry applications.

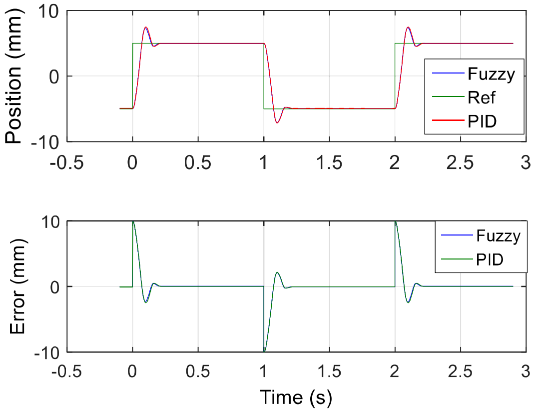

(a) Position response of square wave under fuzzy logic controller.

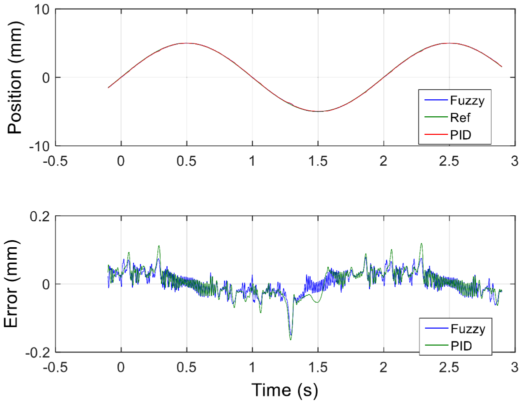

(b) Position response of sinusoidal wave under fuzzy logic controller.

Fig. 10: Position response for sinusoidal and the square wave reference (a) and the sinusoidal wave, under PID and fuzzy logic PD controllers.

IV. CONCLUSION

Fuzzy logic PD control and BP neural network PID control are advanced control algorithms to better performance of complex equipment and nonlinear machines. They inherit the advantages of PID controller, regulating behaviors of control subjects without accurate mathematic modes. Apart from this merit, these advanced control systems can adjust their control parameter according to the variations of the status of the entire control system, overcoming shortcomings of traditional PID control that fails to conquer the influences from varied references and interferences of the environment. Advanced control systems could dominate industrial equipment for intelligence factories and smart mobility.

REFERENCES

[1] Wen Yu, *Recent Advances in Intelligent Control Systems*, Springer Dordrecht Heidelberg London New York, 2009.

[2] J. F. Pan, N.C. Cheung, Yu. Zou, "An Improved Force Distribution Function for Linear Switched Reluctance Motor on Force Ripple Minimization with Nonlinear Inductance Modeling", IEEE Trans. Magn., Vol. 48, no.11, 2012, pp. 3064-3067.

[3] G. El-Saady, El-Nobi A. Ibrahim, M. Abuelhamd, "Hybrid PD-Fuzzy controller for high performance linear switched reluctance motor under different operating conditions", 2016 Eighteenth International Middle East Power Systems Conference (MEPCON), 2016, pp. 437-444.

[4] R. Zhong, Y. B. Wang, Y. Z. Xu, "Position sensorless control of switched reluctance motors based on improved neural network," IET Electric Power Applications, Vol.6, no.2, 2012, pp.111-121.

[5] Shi Wei Zhao, Norbert C. Cheung, Wai-Chuen Gan, Jin Ming Yang, Jian Fei Pan,"A Self-Tuning Regulator for the High-Precision Position Control of a Linear Switched Reluctance Motor" , IEEE Ind. Electron., vol. 54,no. 5, Oct. 2007.

[6] Jianfei Pan, Siu Wing Or, Yu Zou, Norbert C. Cheung, "Sliding-mode position control of medium-stroke voice coil motor based on system identification observer," IET Electric Power Applications, Vol.9, no.9, 2015, pp.620-627.

ACKNOWLEDGMENT

The author gratefully acknowledge of the financial support of the Research Office, The Hong Kong Polytechnic University under the Project G-YBLH.

Author Index

Submission Details

Only online submission will be accepted. Please first register and submit online. The paper is in double column and is similar to most IET or IEEE journal format. There is no page limit. Any number of pages of more than 6 will be subject to additional charge.

The paper guidelines can be downloaded using the link: http://perc.polyu.edu.hk/apejournal/

Any queries, please contact Prof. Eric Cheng, Publishing Director of APEJ, Dept. of Electrical Engineering, The Hong Kong Polytechnic University, Hung Hom, Hong Kong. Email: eeecheng@polyu.edu.hk Fax: +852-2330 1544

Any secretarial support and production related matters, please contact Dr. James Ho, Power Electronics Research Centre, The Hong Kong Polytechnic University, Hung Hom, Hong Kong. Email: eeapej@polyu.edu.hk Tel: +852-3400 3348 Fax: +852-3400 3343

Publication Details

The Journal will be published 2-3 times a year. The first issue was published in 2007. Response time for paper acceptance is within 3 months.

Financial Charge

All the accepted papers will be printed without charge for 6 or less pages. An additional page charge is HK$100 per page. A hardcopy of the journal will be posted to the corresponding author free of charge. Additional copies of the journal can be purchased at HK$200 each. The charge includes postage and packing.

All Chinese Papers will be subjected to a translational fee of HK$350 per page. It will be charged when the paper is accepted for publication.

Advertising

Advertisement is welcome. Full page advertisement is HK$1000. For colour advertisement, the amount is doubled. All the advertisement will be both posted online in the journal website and hardcopy of the journal.

For advertising enquiries and details, please contact Ms. Anna Chang, eeapej@polyu.edu.hk .
Tel: +852-3400 3348 Fax: +852-3400 3343

For payment, please send your cheque, payable to 'The Hong Kong Polytechnic University, address to Ms. Kit Chan, Secretary of APEJ, Dept. of Electrical Engineering, The Hong Kong Polytechnic University, Hung Hom, Hong Kong.